PLEASE CITE THIS ARTICLE AS DOI: 10.1063/5.0201472

A novel mechanism for ramping bursts based on slow negative feedback in model respiratory neurons

Sushmita Rose John, ¹ Ryan S. Phillips, ² and Jonathan E. Rubin ¹) Department of Mathematics, University of Pittsburgh, Ptttsburgh, PA 15260

²⁾Seattle Children's Research Institute, Seattle, WA 98109

(*Electronic mail: jonrubin@pitt.edu)

(Dated: 22 May 2024)

Recordings from pre-Bötzinger complex (pre-BötC) neurons responsible for the inspiratory phase of the respiratory rhythm reveal a ramping burst pattern, starting around the time that the transition from expiration to inspiration begins, in which the spike rate gradually rises until a transition into a high-frequency burst occurs. The spike rate increase along the burst is accompanied by a gradual depolarization of the plateau potential that underlies the spikes. These effects may be functionally important for inducing the onset of inspiration and hence maintaining effective respiration; however, most mathematical models for inspiratory bursting do not capture this activity pattern. Here, we study how the modulation of spike height and afterhyperpolarization via the slow inactivation of an inward current can support various activity patterns including ramping bursts. We use dynamical systems methods designed for multiple timescale systems, such as bifurcation analysis based on timescale decomposition and averaging over fast oscillations, to generate an understanding of and predictions about the specific dynamic effects that lead to ramping bursts. We also analyze how transitions between ramping and other activity patterns may occur with parameter changes, which could be associated with experimental manipulations, environmental conditions and/or development.

Pre-Bötzinger complex (pre-BötC) respiratory neurons can exhibit activity that gradually ramps in intensity, which could be important in the transition from expiration to inspiration. We use modeling, simulations, and mathematical analysis to investigate a novel, biological realistic mechanism by which individual pre-BötC neurons could produce ramping burst patterns. Specifically, we add an additional negative feedback component to an existing pre-BötC model, we show that this addition yields ramping burst dynamics, and we provide a computational exploration of the robustness of these patterns along with a mathematical analysis of the mechanisms that produce them, using the theory of multiple timescale dynamical systems. This work provides a new computational model for the production of ramping bursts by individual neurons and makes predictions about what electrophysiological features underlie this activity.

I. INTRODUCTION

Typical mammalian respiration is a rhythmic behavior with inspiration, post-inspiration, and late-expiration phases. The inspiratory drive that induces movement of the diaphragm for air intake is primarily determined by activity of a brainstem region called the pre-Bötzinger complex (pre-BötC)¹⁻³. Experiments show that a subpopulation of pre-BötC neurons, which activate during the transition from expiration to inspiration and hence are known as pre-I neurons^{4,5}, play a critical role in respiratory rhythm generation⁶. A significant fraction of pre-I neurons exhibit an endogenous bursting capability when isolated from synaptic inputs; some produce *ramping burst patterns*, which often persist under block of synaptic interactions⁷⁻⁹. As with most bursts, ramping bursts feature spiking or active phases that alternate with silent phases

that lack spikes. Their active phases feature a progressive increase in spike frequency, accompanied by a gradual rise in the plateau potential to which the membrane potential returns between spikes (see e.g., Fig. 1A and data from Yamanishi et al. ¹⁰, Fig. 1E). Despite its functional importance, it is not yet known how pre-inspiratory ramping results from dynamics at the single-neuron level.

Extensive computational and mathematical works have proposed and analyzed models for bursting in the pre-BötC^{12,13}. Many include specific transmembrane ion currents, which experiments have extensively characterized in pre-BötC neurons¹. Most existing models fail to produce the gradual increase in spike frequency and other features of ramping bursts, however (e.g., Figure 1B), despite the prevalence of these patterns in isolated pre-BötC neurons. One recent work¹⁴ showed that modifying an existing pre-BötC model by including potassium ion concentration dynamics allows ramping bursts to emerge. That paper, however, does not fully address the experimental findings because the resulting ramping dynamics occurs over smaller ranges of ionic conductances and external potassium concentrations than those that support ramping in experiments⁸, and ramping bursts in neurons can also occur with smaller variations in extracellular potassium concentrations than those arising with ramping bursts in the previous model¹⁵. Thus, we were inspired to seek an alternative mechanism that, when included within a baseline pre-BötC neuron model, could result in ramping bursts.

This paper presents some of the results of this investigation; see also 16 for an earlier version of some of this work. Specifically, we introduce and analyze what we call the *dynamic spike height model*, which includes a second, slow inactivation component known to be associated with the fast inward sodium current 17. This innovation is motivated by recent observations that changes in spike height and other spike shape features can transition a neuron between spiking and various bursting modes 18,19. In this model, we study how the interac-

PLEASE CITE THIS ARTICLE AS DOI: 10.1063/5.0201472

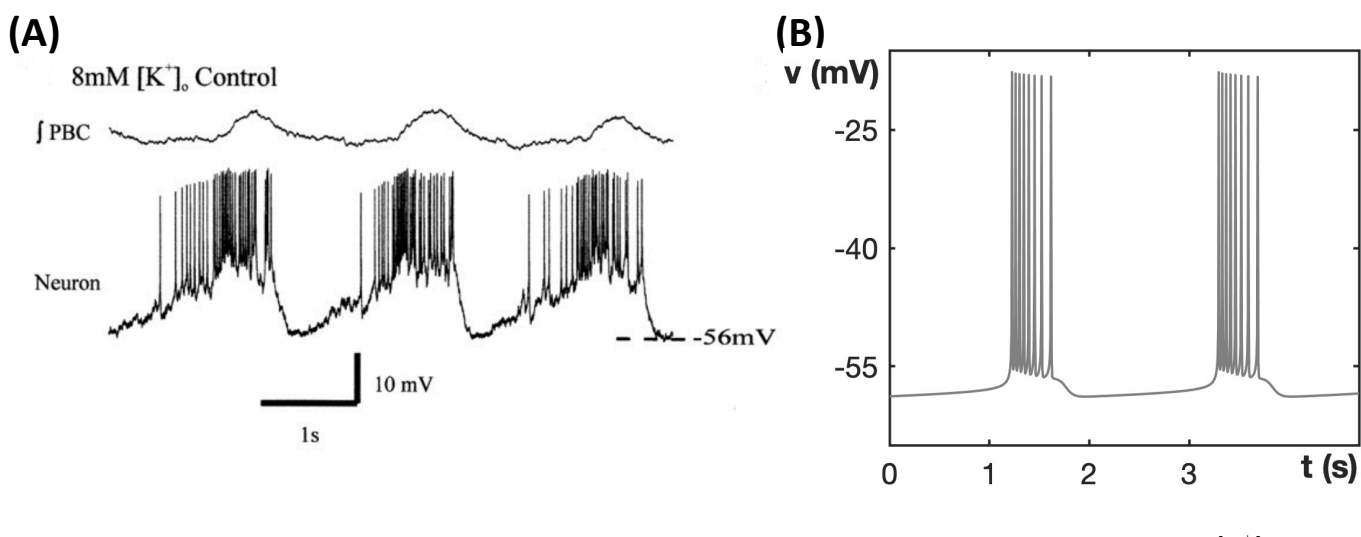


FIG. 1. (A) Ramping burst pattern exhibited by the inspiratory neurons in the pre-BötC at external potassium concentration $[K^+]_o = 8$ mM. This figure was reproduced with permission from J. Neurosci. 23, 3538 (2003). Copyright 2003 Society for Neuroscience. (B) The bursting pattern exhibited by a state-of-the-art model for inspiratory neurons¹¹. Note the gradual decrease in spike frequency within each burst.

tions of ionic currents that evolve on various timescales give rise to several interesting activity patterns, including ramping bursts, depending on the tuning of model parameters. Within the fast-slow decomposition framework often used to analyze multiple timescale dynamical systems²⁰, we use one- and two-parameter bifurcation analysis and averaging over fast subsystem dynamics to explain the mechanisms underlying these activity patterns. In this analysis, we show how the timescale of the secondary inactivation variable of the sodium current, relative to those of other model variables, changes under parameter variations and contributes to the model activity patterns; in particular, in the case of ramping bursts, we find that we must take into account differences in these relations over the course of each burst cycle in order to fully explain the dynamics.

II. METHODS

A. Model system

We consider a single-compartment neuron model, the *dynamic spike height model* or *DSPK model*¹⁶, based on the Hodgkin-Huxley framework²¹. The model includes various voltage-gated currents, a leak current, and a synaptic current. In particular, since we are considering single-cell dynamics, the synaptic current is meant to represent an excitatory tonic drive to the neuron, corresponding to the signals that come to pre-BötC respiratory neurons from other brain areas related to blood pH, pulmonary stretch, and other feedback factors¹². We maintain the conductance of this current at a constant value, which corresponds to a setting of steady metabolic demands and environmental conditions rather than a more dynamic scenario.

The differential equations for the model take the form

$$\begin{cases}
cv' &= -(I_{Na}(v, m_{Na}, h_{Na}, h_{2Na}) + I_{K}(v, n) \\
&+ I_{NaP}(v, h_{NaP}, m_{NaP}) + I_{L}(v) \\
&+ I_{syn}(v)), \\
h'_{Na} &= (h_{Na_{\infty}}(v) - h_{Na})/\tau_{h_{Na}}(v), \\
h'_{2Na} &= (h_{2Na_{\infty}}(v) - h_{2Na})/\tau_{h_{2Na}}(v), \\
m'_{Na} &= (m_{Na_{\infty}}(v) - m_{Na})/\tau_{m_{Na}}(v), \\
n' &= (n_{\infty}(v) - n)/\tau_{n}(v), \\
h'_{NaP} &= (h_{NaP_{\infty}}(v) - h_{NaP})/\tau_{h_{NaP}}(v), \\
m'_{NaP} &= (m_{NaP_{\infty}}(v) - m_{NaP})/\tau_{m_{NaP}}(v),
\end{cases}$$

where I_{Na} is the fast sodium current with activation variable m_{Na} and inactivation variables h_{Na} and h_{2Na} , I_{K} is the delayed rectifier potassium current with activation gate variable n, I_{NaP} is the persistent sodium current with activation variable m_{NaP} and inactivation variable h_{NaP} , I_{L} denotes the leak current and I_{syn} is a synaptic current.

The expressions for the currents in (1) are given by:

$$I_{Na}(v, m_{Na}, h_{Na}, h_{2Na}) = g_{Na} m_{Na}^{3} h_{Na} h_{2Na} (v - e_{Na}),$$

$$I_{K}(v, n) = g_{k} n^{4} (v - e_{K}),$$

$$I_{NaP}(v, m_{NaP}, h_{NaP}) = g_{NaP} m_{NaP} h_{NaP} (v - e_{Na}),$$

$$I_{L}(v) = g_{L} (v - e_{L}),$$

$$I_{syn}(v) = g_{syn} (v - e_{syn}).$$
(2)

The steady-state activation and kinetic functions in (1) are as follows:

PLEASE CITE THIS ARTICLE AS DOI: 10.1063/5.0201472

$$h_{Na\infty}(v) = (1 + e^{-(v_{h_{Na}} + v)/s_{h_{Na}}})^{-1},$$

$$\tau_{h_{Na}}(v) = t_{h_{Na}} \cosh((k_{h_{Na}} + v)/p_{h_{Na}})^{-1},$$

$$h_{2Na\infty}(v) = (1 + e^{-(v_{h_{2Na}} + v)/s_{h_{2Na}}})^{-1},$$

$$\tau_{h_{2Na}}(v) = t_{h_{2Na}} \cosh((k_{h_{2Na}} + v)/p_{h_{2Na}})^{-1}.$$

$$m_{Na\infty}(v) = (1 + e^{-(v_{m_{Na}} + v)/s_{m_{Na}}})^{-1},$$

$$\tau_{m_{Na}}(v) = t_{m_{Na}} \cosh((k_{m_{Na}} + v)/p_{m_{Na}})^{-1},$$

$$n_{\infty}(v) = k_{1}(v)/(k_{1}(v) + k_{2}(v)),$$

$$\tau_{n}(v) = (k_{1}(v) + k_{2}(v))^{-1},$$

$$k_{1}(v) = 0.011(44.0 + v)(1 - e^{(-44.0 - v)/5.0})^{-1},$$

$$k_{2}(v) = 0.17e^{(-v - 49.0)/40.0},$$

$$h_{NaP\infty}(v) = (1 + e^{-(v_{h_{NaP}} + v)/s_{h_{NaP}}})^{-1},$$

$$\tau_{h_{NaP}}(v) = t_{h_{NaP}} \cosh((k_{h_{NaP}} + v)/p_{h_{NaP}})^{-1},$$

$$m_{NaP\infty}(v) = (1 + e^{-(v_{m_{NaP}} + v)/s_{m_{NaP}}})^{-1},$$

$$\tau_{m_{NaP}}(v) = t_{m_{NaP}} \cosh((k_{m_{NaP}} + v)/p_{m_{NaP}})^{-1}.$$

Here, the gating variables n and h_x, m_x for each relevant current label x, including the secondary inactivation gate h_{2Na} of the sodium current I_{Na} as motivated by experimental observations ^{17,22,23}, obey the equations specified in (1).

The default parameter values for the DSPK model are given in Table I. Later in the section, we will discuss further how these were obtained.

B. Non-dimensionalization

We use non-dimensionalization to determine the timescales of the variables in the DSPK model (equations (1), (2)). All variables other than v are gating variables and hence are dimensionless. To make the voltage variable dimensionless, we set $v = VQ_v$, where Q_v is a constant representing an upper bound on the magnitude of v and $V = \frac{v}{Q_v}$ is dimensionless.

Next, we rescale time to make that dimensionless and group parameters^{24,25} so that for each dimensionless voltage or gating variable in the model, call it x, we extract a constant R_x such that the differential equation for x can be written as

$$x' = R_x f_x \tag{4}$$

where the function f_x is $\mathcal{O}(1)$ over the relevant ranges of its arguments.

For all models in this paper, we take $Q_{\nu}=100$. Additional details about the non-dimensionalization process are given in Appendix A; see also¹⁶. Based on the default parameter values for the DSPK model given in Table II, non-dimensionalization yields the timescale constants shown in Table II. Note that we separate out distinct ranges of these values for different values of g_L . As explained in Appendix A, variation of g_L translates into changes in certain timescales that turn out to be important for the model dynamics.

C. Multiple timescale dynamics

Mathematical models for bursting generally have components that evolve on different timescales. Consider a multiple timescale model of the form

$$\begin{cases} dx/dt = f(x, y, \varepsilon), \\ dy/dt = \varepsilon g(x, y, \varepsilon), \end{cases}$$
 (5)

where variables $x \in \mathbb{R}^m, m \ge 2$ and $y \in \mathbb{R}^n, n \ge 2$. We make the assumption that ε is a small timescale parameter, denoted mathematically as $0 < \varepsilon \ll 1$; therefore, y evolves at a slower timescale compared to x.

Letting $\varepsilon \to 0$ gives us the fast subsystem of model (5):

$$\begin{cases} dx/dt = f(x, y, 0), \\ dy/dt = 0, \end{cases}$$
 (6)

in which y remains fixed. The set of equilibrium or critical points of the fast subsystem, which is called the *critical manifold*, has the form

$$\mathcal{M}_0 = \{(x, y) \in \mathbb{R}^m \times \mathbb{R}^n \mid f(x, y, 0) = 0\}.$$

In a neuronal model, points on \mathcal{M}_0 typically correspond either to a non-spiking rest state or to a non-spiking state of depolarization block. In general, we assume that the set \mathcal{M}_0 is composed of a collection of branches, each of the form $\{(x(y),y)\}$ over some range of y values, where f(x(y),y,0)=0.

Rescaling time using $\tau = \varepsilon t$ and then letting $\varepsilon \to 0$ gives us the slow subsystem of model (5):

$$\begin{cases} 0 = f(x, y, 0), \\ dy/d\tau = g(x, y, 0). \end{cases}$$
 (7)

On each branch of \mathcal{M}_0 , system (7) simplifies to

$$\dot{y} = g(x(y), y, 0) \tag{8}$$

where we use the overdot to denote differentiation with respect to τ .

Starting from any initial point not on \mathcal{M}_0 , the solution of (5) for $0 < \varepsilon \ll 1$ will usually converge on the fast or t timescale, based on the dynamics encoded in (6), toward one of the attractors of (6). Once in a small neighborhood of the attractor, the trajectory will evolve under the slow or τ timescale dynamics given approximately by (8), assuming that x = x(y) on the attractor. Under the slow drift, if the trajectory reaches the boundary of the attractor, then the fast subsystem (6) will again become dominant and it will determine how the trajectory transitions to another attractor of this system.

Usually these attractors are either critical points, as discussed above, or periodic orbits, which in neuronal models often correspond to repetitive, tonic spiking dynamics, sometimes called pacemaking. Since the components of *y* are constants in (6), we can plot a bifurcation diagram for this fast

An Interdisciplinary Journal of Nonlinear Science

This is the author's peer reviewed, accepted manuscript. However, the online version of record will be different from this version once it has been copyedited and typeset

PLEASE CITE THIS ARTICLE AS DOI: 10.1063/5.0201472

TABLE I. Default parameter values for DSPK model (1)-(2).

c	36.0 pF	g _{Na}	108.2710 nS	e_{Na}	55.0 mV
$ v_{h_{Na}} $	68.0 mV	$s_{h_{Na}}$	-11.9 mV	$k_{h_{Na}}$	67.5 mV
$p_{h_{Na}}$	-12.8 mV	$t_{h_{Na}}$	8.46 mS	$v_{m_{Na}}$	43.8 mV
$S_{m_{Na}}$	6.0 mV	$k_{m_{Na}}$	43.8 mV	$p_{m_{Na}}$	14.0 mV
$t_{m_{Na}}$	0.25 mS	$v_{h_{2Na}}$	44.3497 mV	$s_{h_{2Na}}$	-1.92387 mV
$k_{h_{2Na}}$	-49.2889 mV	$p_{h_{2Na}}$	4.5524 mV	$t_{h_{2Na}}$	1010.0 mS
g _{NaP}	3.7666 nS	$v_{h_{NaP}}$	60.8242 mV	$k_{h_{NaP}}$	63.5594 mV
Sh_{NaP}	-9.3338 mV	$p_{h_{NaP}}$	9.41933 mV	$t_{h_{NaP}}$	5250.0 mS
$ v_{m_{NaP}} $	47.1 mV	$S_{m_{NaP}}$	3.1 mV	$k_{m_{NaP}}$	47.1 mV
$p_{m_{NaP}}$	6.2 mV	$t_{m_{NaP}}$	1.0 mS	g_K	250.148 nS
e_K	-73.0 mV	g_L	4.0 nS	e_L	-62.5 mV
gsyn	0.3921 nS	e_{syn}	-10.0 mV		

TABLE II. The timescales associated with the variables of the DSPK model (1)-(2) for different g_L values.

$g_L = 3.5$	$R_V \ R_{h_{NaP}} \ R_{h_{2Na}}$	≈ ∈ ∈	$ \begin{array}{c c} 6.94 \\ [10^{-4}, 0.002] \\ [10^{-4}, 0.011] \end{array} $	$R_{h_{Na}} \ R_{m_{NaP}}$	€	[0.24, 0.744] [1.0, 3.5]	$R_{m_{Na}}$ R_n	€	[4.0, 4.78] [0.13, 0.49]
$g_L = 4.0$	$egin{aligned} R_V \ R_{h_{NaP}} \ R_{h_{2Na}} \end{aligned}$	≈ ∈ ∈	$ \begin{array}{c c} 6.94 \\ [10^{-4}, 0.006] \\ [10^{-4}, 0.11] \end{array} $	$R_{h_{Na}} \ R_{m_{NaP}}$	€	[0.167, 1.7] [1.0, 19.20]	$R_{m_{Na}}$ R_n	€	[4.0, 8.45] [0.06, 0.7]
$g_L = 4.6$	$egin{aligned} R_V \ R_{h_{NaP}} \ R_{h_{2Na}} \end{aligned}$	≈ ∈ ∈	$ \begin{array}{c c} 6.94 \\ [10^{-4}, 0.0079] \\ [10^{-4}, 0.2] \end{array} $	$R_{h_{Na}} \ R_{m_{NaP}}$	€	[0.166, 2.07] [1.0, 28.84]	$R_{m_{Na}} \ R_n$	€	[4.0, 9.94] [0.058, 0.739]

subsystem by using any component of y as a bifurcation parameter. A bifurcation diagram helps us to predict the attractors to which the fast dynamics will evolve, depending on the initial conditions. If we consider the slow drift given by (8) along a branch $\{x=x(y)\}$ of attracting critical points, then we can also predict how trajectories will move along such a branch, when this branch will end and another fast transition will occur, and which attractor will be the target of this fast transition.

Until now, we have ignored the complication that a fast system attractor may be a periodic orbit, which cannot simply be represented by a single curve $\{x = x(y)\}$ parameterized by y. Using the slow subsystem, we can calculate the average behavior of the slow variables on a stable periodic orbit of the fast subsystem. Suppose that for each y in some domain, $x_P(y;t)$ is a stable periodic orbit of the fast subsystem (6) with period T(y). The averaged slow subsystem on this domain is given by

$$dy/d\tau = \frac{1}{T(y)} \int_0^{T(y)} g(x_P(y;t), y, 0) dt.$$
 (9)

We can use system (9) to determine how the slow variables will drift along such an attracting family of periodic orbits of

the fast subsystem. In some cases, this may occur until the family ends and another fast transition results. On the other hand, averaging theory explains that a hyperbolic critical point of the averaged slow system (9) corresponds to a periodic orbit in the full system (5) for ε sufficiently small, so when such a point exists and is stable, our fast-slow analysis predicts that the full model will engage in periodic dynamics.

D. Ramping dynamics and parameter tuning

We categorize a ramping burst pattern as one in which the spike frequency increases as the burst progresses while the hyperpolarization between spikes weakens (Figure 1A). To find parameter values for (1) that yield ramping burst patterns, we harnessed an optimization routine using the *fminsearch* command in MATLAB. The cost function that we implemented in the minimization algorithm is the sum of the following components:

- (1) $\sum_{k=1}^{N-2} (ISI_{k+1}/ISI_k)$, the sum of the ratios of successive inter-spike intervals,
- (2) $\sum_{k=1}^{N-1} (\text{Tr}_{k+1}/\text{Tr}_k)$, the sum of the ratios of minimal voltages, or voltage troughs, across successive spikes,

PLEASE CITE THIS ARTICLE AS DOI: 10.1063/5.0201472

• (3) $\min(\operatorname{Sp}_k, k \in 1, 2, \dots, N)/\operatorname{Sp}_1$, the ratio between the minimum of the voltages across all spike peaks and the peak voltage of first spike (note here that these voltages were always negative, so their ratio was positive and became larger if the shortest peak became shorter, with a more negative peak voltage), and

• (4) $\max(\mathrm{ISI}_k, k \in 1, 2, \dots, N)$ /(silent phase duration of the burst),

where the N is the number of spikes in the burst. That is, the cost function penalizes increases in ISI durations (1), deepening of spike troughs (2), excessive shrinkage of spike height at any stage of the burst (3) – since we chose to avoid close approach to depolarization block for these patterns – and overly long ISIs within the active phase of a burst (4). After tuning model parameters by hand to obtain an approximate ramping pattern, this minimization algorithm helped us to identify parameter values for which the models exhibit ramping burst dynamics that align with the qualitative characteristics observed experimentally. In the supplementary material we show that the many significant digits in the values in Table I are not necessary for ramping burst dynamics; moreover, we explicitly investigate robustness with respect to variation of biologically central parameter values in the Results section of the paper.

E. Code Accessibility

Model (1)-(3) was implemented using the XPPAUT software²⁶ and the simulations were performed on a standard pc laptop (macOS, 1.4 GHz Quad-Core Intel Core i5 Processor, 8GB RAM). The files used to simulate the model as well as the MATLAB code used for parameter optimization are freely available online at https://modeldb.science/2016216. We note that data sharing is not applicable to this article as no new data were created or analyzed in this study.

III. RESULTS

A. The DSPK model produces a gradual ramping burst pattern

The default parameter values for the DSPK model are given in Table I. When the parameters take these values, the model exhibits a ramping bursting pattern (Figure 2). The parameter values in Table I were obtained from running an optimization routine in MATLAB, which led to the specification of some of these values to several significant digits, and we can vary them away from these values without significantly affecting the ramping pattern. A ramping bursting pattern exhibited by the model for parameter values having at most two decimal point precision is shown in the supplementary material, Figure S1. The optimization routine in MATLAB found the parameter values in Table I by penalizing an increase in inter-spike intervals, a decrease in the strength of depolarization and an increase in the hyperpolarization depth across the burst.

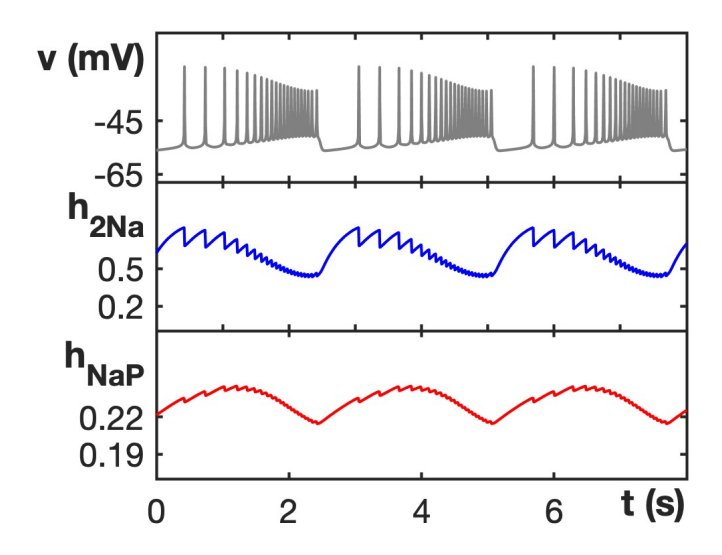


FIG. 2. Ramping burst pattern exhibited by the DSPK model (1)-(2) for default parameter values given in Table I. Ramping bursting pattern exhibited by the DSPK model (1), (2) when parameter values are rounded to a maximum precision of two decimal points is shown in Sup.

Notice that the ramping burst produced with the optimized parameter values (Figure 2) starts with relatively slow spikes. After a small number of these events, the spiking oscillations increase in frequency. In parallel, the minimum voltages associated with successive spikes become less negative, providing the desired ramping shape to the voltage plateau on top of which spikes arise. While h_{NaP} exhibits net deinactivation across the slow spikes and only starts to inactivate once the spikes become sufficiently fast, h_{2Na} , on average, declines on every spike, such that the initial growth in I_{NaP} is approximately balanced by the decline of I_{Na} and thus spikes do not accelerate too quickly. While the model successfully produces ramping bursts for an optimal parameter set, we would like to know how robust this behavior is as well as what dynamic mechanisms are involved in producing the ramping bursts and the other activity patterns to which the ramping bursts give way as parameters are varied sufficiently. We explore these topics computationally and mathematically in the rest of this section.

B. Dynamic regimes of the DSPK model are demarcated by bifurcation events

Past works have explored the dependence of bursting dynamics in respiratory neurons on the leak and persistent sodium current conductances, g_L and $g_{NaP}^{14,27-29}$. Hence, to begin our analysis, we simulated the DSPK model across a range of g_L and g_{NaP} values and applied an automatic procedure to classify the resulting dynamics into one of five forms: ramping bursts (red), bursting without a ramping pattern (blue), tonic spiking (black), silent with a stable critical point at a low voltage, and depolarization block with a stable critical point at a high voltage (Figure 3A). We wrote a

PLEASE CITE THIS ARTICLE AS DOI: 10.1063/5.0201472

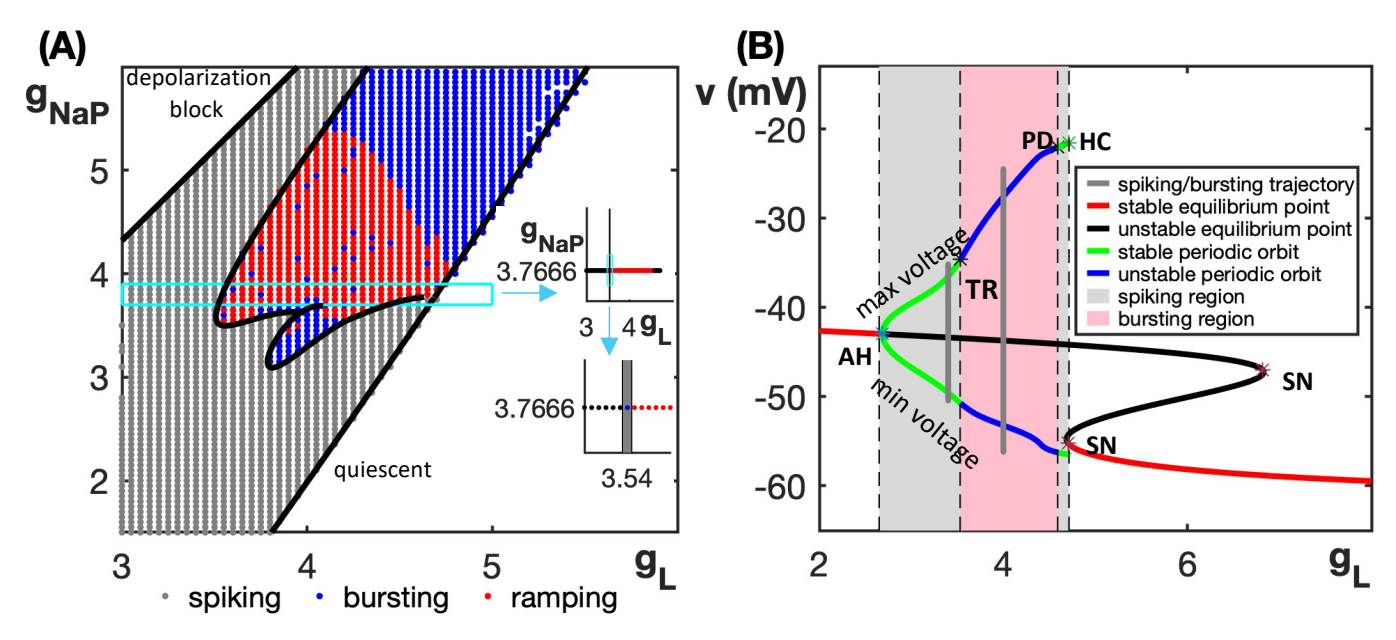


FIG. 3. Activity patterns in the DSPK model. (A) Classification of the activity patterns exhibited by model (1), (2) for different g_{NaP} and g_L values. The inset highlights at two levels of zoom the transition from spiking (black) to ramping bursts (red) and back to spiking as g_L increases for $g_{NaP}=3.7666$. For a small region near $g_L=3.54$ (shaded grey), the model exhibits amplitude modulated spiking. (B) Bifurcation diagram of the full model (1), (2) with respect to g_L with $g_{NaP}=3.7666$. The g_L values of certain key bifurcations are indicated with vertical, dashed black lines. The model undergoes a torus bifurcation (TR) at $g_L\approx3.534$ nS, where the periodic orbits (green/blue branches) change stability and a branch of stable tori (not shown) originates. It further undergoes a period doubling (PD) bifurcation at $g_L\approx4.6$. Note that the lower g_L values where the model has a stable equilibrium point and where the torus bifurcation occurs are not included in panel (A), which focuses on the bursting regions. AH: Andronov-Hopf bifurcation, SN: Saddle node bifurcation, HC: homoclinic bifurcation, TR: Torus bifurcation, PD: Period doubling bifurcation. The boundary curves separating the different activity patterns in panel (A) were obtained from two parameter continuation of SN, AH, TR, and PD bifurcations as shown in (B). The absolute values of the derivatives of h_{NaP} , h_{2Na} , and n along the stable oscillation pattern for several g_L values are shown in the supplementary material in Figure S2.

custom MATLAB code to detect the types of patterns associated with the different g_L and g_{NaP} values; see Section IID for details on how ramping bursts were specified. Although the identification fails at isolated points as can be seen in Figure 3A, it generally performs well. We note that the small, second, blue (non-ramping) bursting region at low g_{NaP} corresponds to bursts with small numbers of spikes. Note that in exploratory simulations, we did not see any clear indications of bistability within the parameter domain considered. Although the region of the slice of parameter space in which ramping bursts occur is bounded and only spans about 1 nS of change in each of g_{NaP} and g_L , this represents a more robust form of ramping with respect to changes in g_L than that based on potassium concentration dynamics¹⁴, and the bursting region can be expanded by varying certain parameters jointly (see Section III H).

Figure 3B shows the bifurcation diagram of the full DSPK model (1)-(3) with respect to g_L for g_{NaP} fixed at its default value of 3.7666 nS. For sufficiently low g_L , the model has a stable critical point (red) corresponding to pinning or depolarization block at a relatively depolarized voltage. As g_L increases, we see that the model undergoes a supercritical AH bifurcation, resulting in a family of stable periodic orbits (green curves) corresponding to tonic spiking. These periodic orbits lose stability at a torus bifurcation at $g_L \approx 3.534$ nS. A branch of stable tori originates at this g_L value, corresponding

initially to solutions that still feature tonic spiking but with spike amplitudes that vary gradually with a second, slower period (see subsection III C); although we do not expect these solutions to be very robust to parameter changes or of direct biological significance, they represent the start of the dynamic transition that eventually results in bursting for larger g_L .

Above the torus bifurcation, we observe bursting and then, for still larger g_L , a period doubling (PD) bifurcation gives rise to a second small interval of tonic spiking periodic orbits, which ends in a homoclinic (HC) bifurcation. This bifurcation occurs close to a saddle-node bifurcation of critical points and these may in fact coincide in a SNIC bifurcation; in any case, for g_L above this level, system trajectories settle to a silent, hyperpolarized equilibrium state. The boundary curves between the various activity patterns in Figure 3A were obtained through two parameter continuation of different bifurcations indicated in Figure 3B. The curve of AH bifurcations marked the transition from depolarization block to spiking. Proceeding in the direction of increasing g_L , TR and PD bifurcations gave the boundary separating bursting and spiking regions. Lastly, at largest g_L , SN bifurcations marked the transition from spiking to a quiescent state. The bifurcation diagram in Figure 3B and corresponding sequence of activity patterns are consistent with our numerically observed lack of bistability of system solutions; however, the simple, full system bifurcation diagram in Figure 3B does not give us much

PLEASE CITE THIS ARTICLE AS DOI: 10.1063/5.0201472

information about the activity patterns occurring for most of the range of g_L values between the torus and PD bifurcations. To understand these, we will perform a fast-slow timescale decomposition and additional dynamical systems analysis in subsection III C.

C. Timescales in the DSPK model vary with g_L

We will now perform a deeper investigation of the diverse activity patterns that the DSPK model exhibits for $g_{NaP}=3.7666$ nS for various values of g_L . Figure 3A shows that the activity pattern changes from spiking for low g_L values to ramping bursts for intermediate g_L to another phase of spiking for higher g_L values. In fact, numerical simulations show that before transitioning to bursting, the model also exhibits amplitude modulated fast spiking for a small range of g_L values near 3.54 nS. Therefore, in the rest of this section we analyze in detail the regular spiking, amplitude modulated spiking, ramping bursts, and additional forms of spiking exhibited by the model for $g_{NaP}=3.7666$ nS. For convenience, we will henceforth drop the units of nS when we refer to specific conductance values.

Note that along the family of oscillatory solutions of the DSPK model, the oscillations feature larger maximal voltage and more negative minimal voltage for larger g_L (Figure 3B, green and blue curves). We can explain this observation heuristically based on the properties of the currents in the model. I_L is a hyperpolarizing current due to its reversal potential, so increasing g_L lowers the membrane potential between spikes and reduces excitability and spike frequency. Due to the increased time interval and reduced voltage between spikes, I_{Na} and I_{NaP} will have more time to recover from inactivation and will tend towards greater recovery from inactivation due to the voltage-dependent properties of their inactivation gates, h_{Na} and h_{NaP} . At the same time, the magnitude of I_{Na} and I_{NaP} deinactivation needed to overcome I_L and generate a spike increases with g_L . Therefore, as g_L increases, I_{Na} and I_{NaP} are more recovered from inactivation at spike initiation, which leads to stronger spike-generating currents and taller spikes that reach larger values of v_{max} . In turn, these taller spikes cause greater activation of the outward current I_K , causing larger spike afterhyperpolarizations (i.e., more negative v_{min}) as g_L is increased.

Since the rate of change of h_{2Na} depends on v in (1), the increase in the range of v values that occurs during oscillations for larger g_L results in an acceleration of the timescale on which h_{2Na} evolves. To see this, we turn to non-dimensionalization of the DSPK model; information about this process for different values of g_L is shown in the subsection II B. We find that h_{NaP} evolves on a slow timescale for all values of g_L , while the m-variables, h_{Na} , n, and v remain

(relatively) fast for all g_L . For g_L sufficiently small, h_{2Na} can also be considered as slow. However, as g_L is increased to 4, the timescale of h_{2Na} becomes less clear. We consider the relation between the timescales of h_{2Na} and the other variables in the model to determine how to treat h_{2Na} in our mathematical analysis. Figure S2 in the supplementary material shows the absolute values of the t-derivatives of h_{NaP} , which is a slow variable, n, which is the slowest among the fast variables in the DSPK model (1)-(3), and h_{2Na} , along the stable activity patterns observed for several values of g_L . We see that the rate of change of h_{2Na} is close to that of the slow variable h_{NaP} for $g_L = 3.5$ and closer to that of the fast variable n for $g_L = 4.6$. Hence, we will treat h_{2Na} as having an intermediate timescale for $g_L = 4$ and a fast timescale for $g_L = 4.6$. We shall see that this choice fits well with the dynamic behavior of the model variables as we turn to the analysis of the model's activity patterns for these g_L values below, in the remaining parts of this section.

D. Fast oscillations and a stable fixed point in the slow averaged dynamics yield tonic spiking in the DSPK model for $g_L=3.5$

When g_L =3.5, the model generates rapid tonic spiking as shown in Figure 4A. From non-dimensionalization, we conclude that in this case, both h_{NaP} and h_{2Na} can be considered to be slow variables. Therefore, the model for g_L =3.5 can be studied as a 5-fast $(v, m_{Na}, m_{NaP}, h_{Na}, n)$ and 2-slow variable system.

To perform a fast-slow decomposition on a system with 2 slow variables, we typically start by fixing one of the slow variables and generating the bifurcation diagram of the fast subsystem with respect to the other. In this case, the choice of which slow variable to fix is not so important because in direct simulations of (1), (2) with $g_L = 3.5$, we see that both h_{2Na} and h_{NaP} remain relatively constant throughout each spike (Figure 4A; notice the highly zoomed y-axis range shown for h_{NaP}). For consistency with the next subsection, we fix $h_{NaP} = 0.163$ and use h_{2Na} as our bifurcation parameter for the fast subsystem, given by the differential equations for $v, m_{Na}, m_{NaP}, h_{Na}, n$. The resulting bifurcation diagram is shown in Figure 4B with the spiking trajectory for $g_L = 3.5$ superimposed in grey. Notice that the spiking trajectory corresponds to a stable periodic orbit in the fast subsystem.

To build on our observations in Figure 4A-B, we next plot the two-parameter bifurcation diagram of the fast subsystem with respect to the two slow variables, h_{2Na} and h_{NaP} (Figure 4C). We also calculate and plot the slow averaged nullclines for the slow subsystem, generated by averaging over the fast subsystem oscillations (see Section II C). Specifically, when we average over the fast spikes, the slow averaged system of equations is given by

This is the author's peer reviewed, accepted manuscript. However, the online version of record will be different from this version once it has been copyedited and typeset





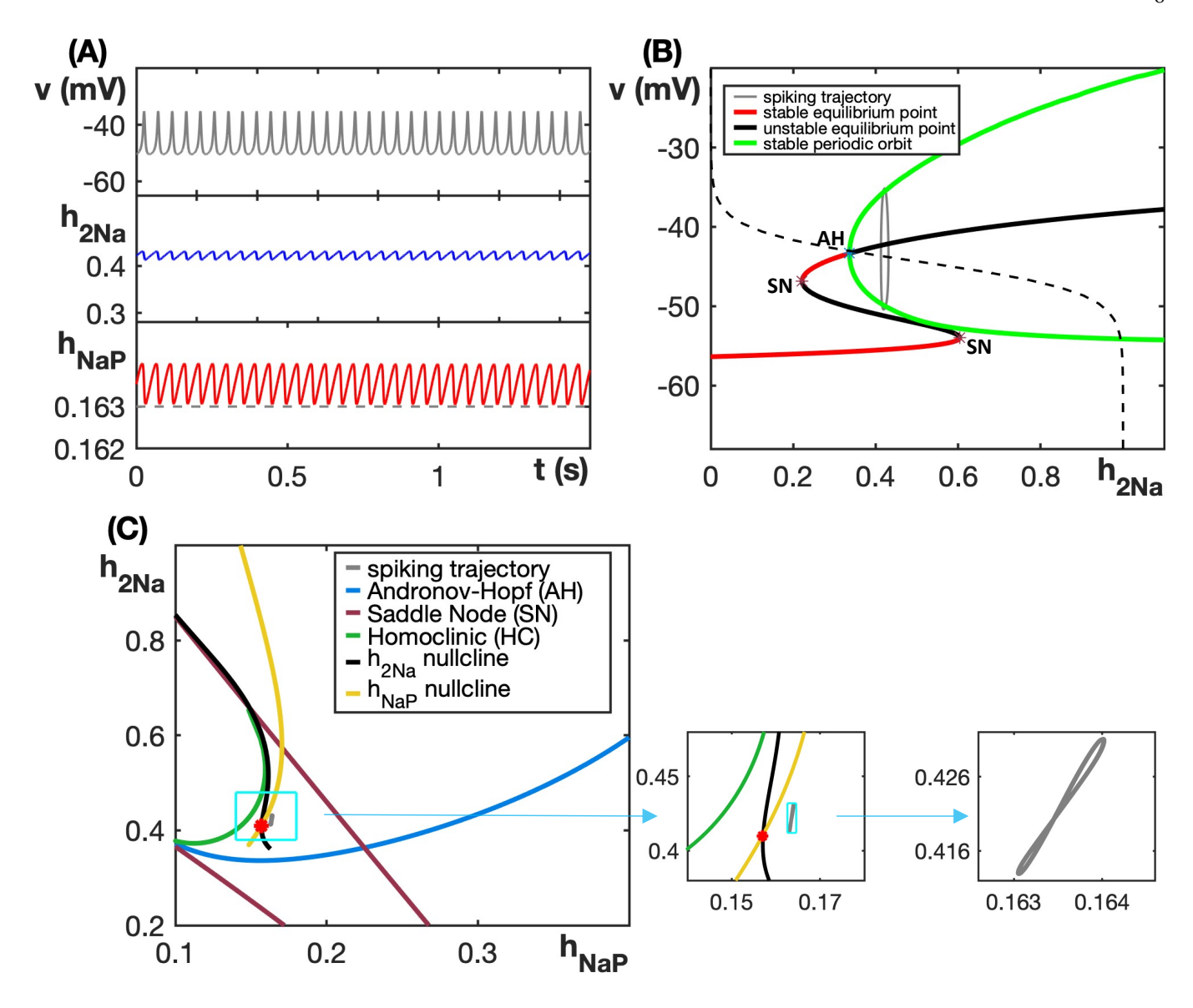


FIG. 4. Analysis of DSPK the model (1), (2) for $g_L = 3.5$. (A) Spiking pattern exhibited by the DSPK model (1), (2) for $g_L = 3.5$. The dashed grey line in the lowest panel corresponds to $h_{NaP} = 0.163$. (B) Bifurcation diagram of the fast subsystem with respect to h_{2Na} for $h_{NaP} = 0.163$. AH: Andronov-Hopf bifurcation, SN: Saddle node bifurcation. (C) The two-parameter bifurcation diagram of the fast subsystem with respect to h_{2Na} and h_{NaP} . The slow averaged nullclines of h_{2Na} and h_{NaP} are shown in black and yellow, respectively. These are relevant in the region where the fast subsystem exhibits oscillations, which lies between the homoclinic curve (green) and AH curve (blue) for the subsystem. For completeness, we also show the system's SN curves (magenta). In both (B) and (C), the spiking trajectory is overlaid in grey, but since it is difficult to see in (C), where the spiking trajectory lies very close to the fixed point of the slow averaged system (red asterisk), the insets show a zoomed view of this region.

$$h'_{NaP} = \frac{1}{T(h_{NaP}, h_{2Na})} \int_{0}^{T(h_{NaP}, h_{2Na})} \left(\frac{h_{NaP\infty}(v(t; h_{NaP}, h_{2Na})) - h_{NaP}}{\tau_{h_{NaP}}(v(t; h_{NaP}, h_{2Na}))} \right) dt$$

$$h'_{2Na} = \frac{1}{T(h_{NaP}, h_{2Na})} \int_{0}^{T(h_{NaP}, h_{2Na})} \left(\frac{h_{2Na\infty}(v(t; h_{NaP}, h_{2Na})) - h_{NaP}}{\tau_{h_{2Na}}(v(t; h_{NaP}, h_{2Na}))} \right) dt$$
(10)

where $v(t; h_{NaP}, h_{2Na})$ is the *v*-coordinate along the stable periodic orbit of the fast-subsystem for fixed h_{NaP} and h_{2Na} , with period $T(h_{NaP}, h_{2Na})$ with respect to the time variable *t*.

The equations (10) are valid over the range of (h_{NaP}, h_{2Na}) values where there are stable oscillations in the fast subsystem. In Figure 4C, this corresponds to the parameter range

PLEASE CITE THIS ARTICLE AS DOI: 10.1063/5.0201472

located to the right side of the HC curve (shown in green) and to the left side of AH curve (shown in blue). We see that the slow averaged nullclines intersect at a fixed point very near $h_{2Na} \approx 0.45$ with $h_{NaP} \approx 0.163$ (Figure 4C, red dot). Moreover, the relative slopes of the slow averaged nullclines at this fixed point, which lies on the left branch of the cubic-like h_{2Na} averaged nullcline (Figure 4C, black curve), imply that it is stable, consistent with the numerical results. Averaging theory tells us that this fixed point corresponds to a stable periodic orbit in the full system.

Since it is a projection to the slow phase space, the full oscillation in the fast variables, shown in Figure 4A-B, is not visible in Figure 4C. We note that if we define ε so that the slow time variable τ satisfies $\tau = \varepsilon t$, then we expect to observe an $\mathcal{O}(\varepsilon)$ error in the position of the fixed point computed from the averaged nullclines, since they are calculated assuming h_{NaP} and h_{2Na} to be fixed, as well as an $\mathcal{O}(\varepsilon)$ drift in each slow variable along each spike. Indeed, the projection of the actual spiking trajectory to the (h_{NaP}, h_{2Na}) plane lies very close to, but not exactly at, the nullcline intersection point (Figure 4C, grey versus red). Combining the panels in Figure 4, we have a full fast-slow analysis of the mechanisms involved in producing the fast spiking trajectory for g_L =3.5.

E. Destabilization of the slow averaged fixed point yields amplitude modulated spiking in the DSPK model for $g_L = 3.54$

When g_L is increased to 3.54, the model exhibits amplitude modulated (AM) spiking, as shown in Figure 5A. The timescale of h_{2Na} does not vary much from the previous case since there is little difference between the g_L values in these cases. Hence, for $g_L = 3.54$, the model can again be analyzed as a 5-fast and 2-slow variable system.

Following the approach from the previous case, we extract the approximation $h_{NaP} \approx 0.168$ from the simulation in Figure 5A, fix h_{NaP} there, and consider the one-parameter bifurcation diagram of the fast subsystem with respect to h_{2Na} (Figure 5B). Note that, although the bifurcation diagram looks almost identical to the previous one (Figure 4B), the superimposed full system trajectory no longer approximates the path of a single fast subsystem periodic orbit. Indeed, this trajectory, depicted in grey, drifts back and forth along a segment of the stable periodic orbit family of the fast subsystem, reversing direction periodically. From this observation, we conclude that fixing h_{NaP} does not provide a useful representation of the system dynamics; indeed, the direction reversals require nontrivial dynamics in a pair of slow variables. Nonetheless, the one-parameter bifurcation diagram gives us a starting point from which to generate a two-parameter bifurcation diagram of the fast subsystem with respect to the two slow variables h_{2Na} and h_{NaP} , to which we now turn.

Within the two-parameter bifurcation diagram (Figure 5C), we also superimpose the full system trajectory (grey) and the slow averaged nullclines from system (10) with $g_L = 3.54$. Although the slow averaged nullclines again intersect at a fixed point (red dot), this point lies on the middle branch of the cubic-like h_{2Na} averaged nullcline and is unstable, with a sta-

ble periodic orbit of system (10) around it. That is, it appears that there has been a supercritical AH bifurcation of the slow averaged system as g_L has increased from 3.5 to 3.54. At or near the g_L value where this AH bifurcation occurs, numerical simulations show that the full system undergoes torus bifurcation (Figure 3B). We also note that the resulting periodic solution passes near a curve of homoclinic bifurcations as h_{2Na} approaches and reaches its maximum (Figure 5C), which explains the slowing of spiking along this part of the solution (Figure 5A).

In summary, for $g_L=3.54$, the fast dynamics of model (1), (2) is attracted to the stable family of fast subsystem periodic orbits, which is parameterized by h_{NaP} and h_{2Na} . The corresponding slow averaged system (10) exhibits its own stable oscillations; each such oscillation cycle represents a path along the fast subsystem periodic orbit family along which the fast variables are dragged. This situation results in ongoing spiking but with a periodic modulation of the amplitude of the spikes produced (Figure 5A). In biological terms, the AM spiking pattern results from a complex interplay of activation and (de)inactivation of the I_{Na} and I_{NaP} currents, which is only observed for a small range of g_L values.

F. Dynamics on three timescales give rise to ramping bursts in the DSPK model for $g_L = 4\,$

The ramping burst pattern exhibited by the model (1)- (3) for $g_L = 4$ is displayed in Figure 2. Non-dimensionalization shows that for $g_L = 4$, the timescale constant for h_{2Na} is greater than that of the previous cases (see subsection II B and supplementary material Figure S2). In this case, we analyze h_{2Na} as having an intermediate timescale, with h_{NaP} remaining slow and the other five variables remaining fast.

We analyze the case with $g_L = 4$ in several steps. Specifically, we divide the bursting time course into four parts as shown in Figure 6A and analyze each epoch, or region, separately. In Regions I and II, the trajectory is colored grey and pink, respectively. Region III comprises the cyan and orange shaded parts of the bursting trajectory and the trajectory is colored purple in Region IV. With three timescales in the system, we can first treat the slow variable h_{NaP} as a bifurcation parameter and consider the dynamics of the remaining, fastintermediate variables. If we therefore consider the bifurcation diagram of the fast-intermediate subsystem with respect to h_{NaP} (Figure 6B), we find that the fast-intermediate subsystem has stable periodic orbits (green) for h_{NaP} values between 0.18 and 0.24, while it has a stable equilibrium point corresponding to depolarization block for each larger h_{NaP} value, all of which will be useful later.

It is important to keep in mind that this bifurcation diagram shows us the attractors of the fast-intermediate system with h_{NaP} fixed. In reality, h_{NaP} does have a slow drift, which will play a role in shaping the overall system dynamics. Indeed, due to this slow drift, we do not show the bursting solution superimposed on the bifurcation diagram in Figure 6B. That is, because h_{NaP} increases and decreases again during different parts of the active phase of each ramping burst (Regions I

This is the author's peer reviewed, accepted manuscript. However, the online version of record will be different from this version once it has been copyedited and typeset

PLEASE CITE THIS ARTICLE AS DOI: 10.1063/5.0201472

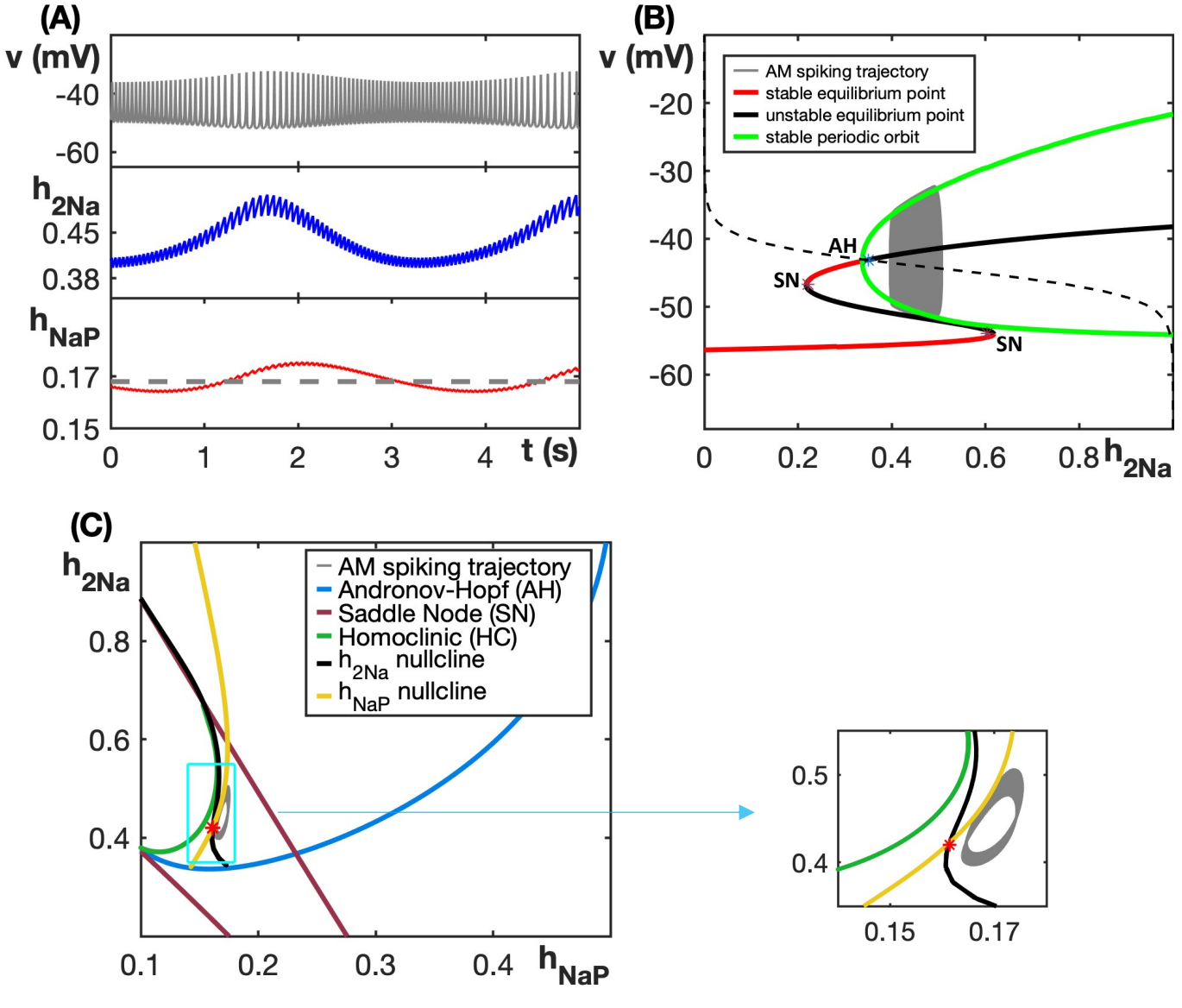


FIG. 5. Analysis of DSPK the model (1), (2) for $g_L = 3.54$. (A) Amplitude modulated (AM) spiking pattern exhibited by the DSPK model. The dashed grey line in the lowest panel corresponds to $h_{NaP} = 0.168$. (B) Bifurcation diagram of the fast subsystem with respect to h_{2Na} for $h_{NaP} = 0.168$. AH: Andronov-Hopf bifurcation, SN: Saddle node bifurcation. (C) The two-parameter bifurcation diagram of the fast subsystem with respect to h_{2Na} and h_{NaP} . The slow averaged nullclines of h_{2Na} and h_{NaP} are shown in black and yellow respectively. The fixed point in the slow averaged system is shown as a red asterisk and the inset shows a zoomed view near this point. In both (B) and (C), the AM spiking trajectory is overlaid in grey.

and III in Figure 6A, respectively), the bursting pattern is not apparent when this trajectory is shown in this projection.

With the bifurcation diagram in Figure 6B established, we turn to the fast-intermediate subsystem. For the analysis of the fast-intermediate dynamics with h_{NaP} fixed, we should start by treating h_{2Na} as a bifurcation parameter and considering the dynamics of the fast variables. Once we determine the attracting dynamics for the fast variables, we can take into account the intermediate timescale drift of h_{2Na} . Once this combined analysis reveals the attracting dynamics for the combined fast-intermediate system for each h_{NaP} , we can consider how slow drift in h_{NaP} results in passage along the fast-

intermediate timescale attractors and possibly jumps on the faster timescales to other attractors. Let us now analyze the dynamics in each of the regions.

Region I: The spiking, active phase of the burst begins at the start of this region (dark grey part of time course in Figure 6A). Within this region, the burst pattern in Figure 6A exhibits slow spikes. Notice that h_{2Na} oscillates up and down on each cycle with little net change while h_{NaP} shows an increasing trend across successive cycles. Also notice that the values of h_{NaP} here correspond to a range, from about 0.225 to 0.24, on which the fast-intermediate system has stable periodic orbits in Figure 6B. Thus, we turn to the fast-intermediate system to

An Interdisciplinary Journal of Nonlinear Science This is the author's peer reviewed, accepted manuscript. However, the online version of record will be different from this version once it has been copyedited and typeset



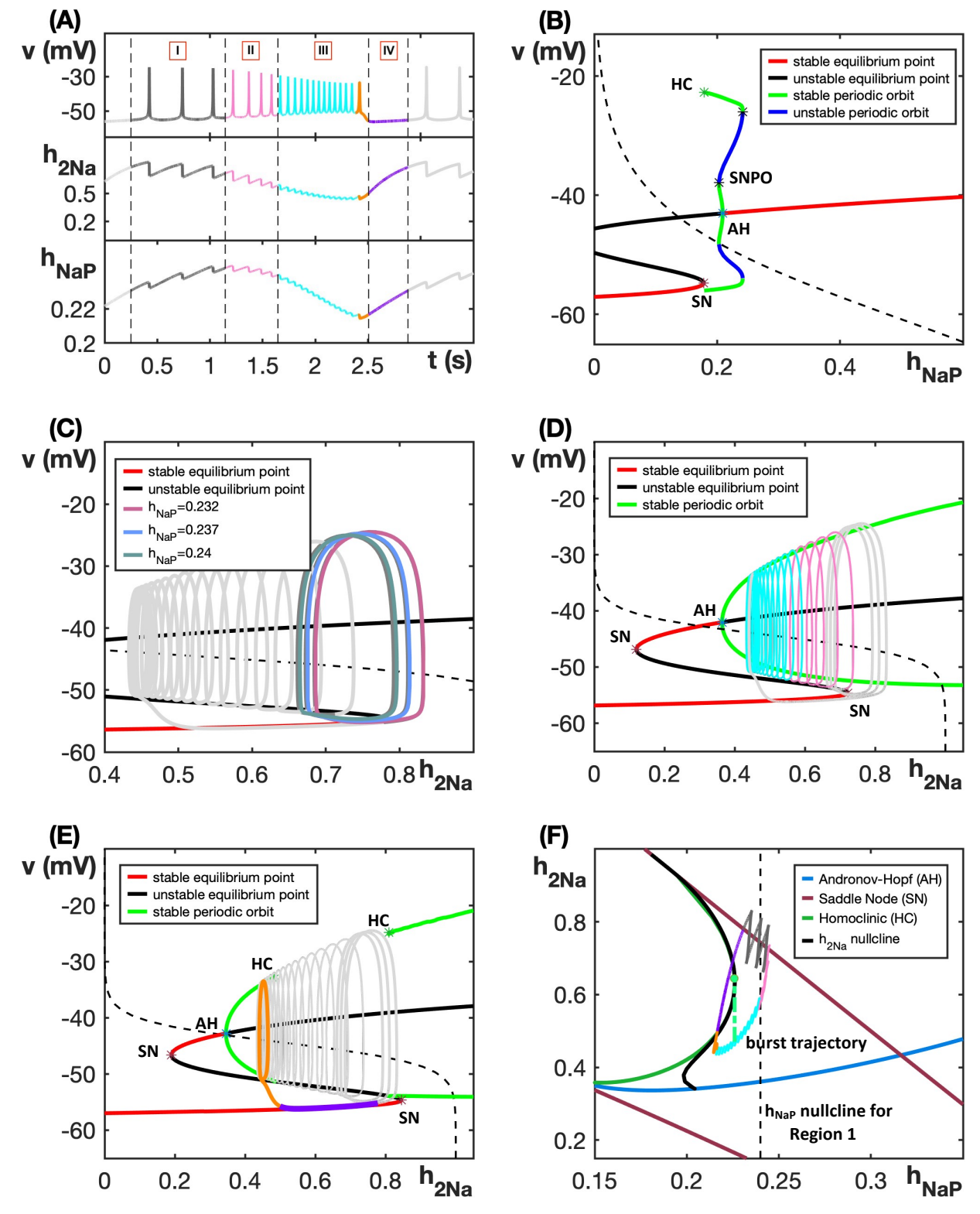


FIG. 6. (A) Ramping burst pattern exhibited by the DSPK model (1)-(3) for $g_L = 4$. To analyze the burst further, we divide it into different regions as shown. (B) The bifurcation diagram of the fast-intermediate subsystem with respect to h_{NaP} . (C) Comparison of the periodic orbits of the fast-intermediate system for different h_{NaP} values with the slow oscillations in Region I of the bursting pattern for $g_L = 4$, comprising part of the projection of the full ramping burst solution (light grey). (D-E) Bifurcation diagram of the fast subsystem with respect to h_{2Na} for (D) $h_{NaP} = 0.245$ and (E) $h_{NaP} = 0.215$. AH: Andronov-Hopf bifurcation, SN: Saddle node bifurcation, HC: homoclinic bifurcation, SNPO: Saddle node of periodic orbits. The h_{2Na} -nullcline is shown as dashed black curve in each case. (F) The two-parameter bifurcation diagram of the fast subsystem with respect to h_{2Na} and h_{NaP} for $g_L = 4$. The slow averaged nullcline of h_{2Na} averaged over the oscillations in the fast subsystem is shown in solid black. The slow averaged nullcline of h_{NaP} averaged over the oscillations in the fast-intermediate subsystem in Region I is shown in dashed black. The green dashed line marks the maximal h_{NaP} value for which homoclinic bifurcations split the family of fast subsystem periodic orbits. In each of (C)-(F), the ramping burst trajectory (light grey) is overlaid with the relevant section colored.

PLEASE CITE THIS ARTICLE AS DOI: 10.1063/5.0201472

understand the nature of these orbits, and then we consider the drift in h_{NaP} across successive orbits.

A comparison of the tonic spikes in this region of the burst to the stable periodic orbits in the fast-intermediate system, projected onto the fast v and intermediate h_{2Na} coordinates, is shown in Figure 6C. From this diagram, we see that each of the three spikes in Region I corresponds to an orbit in the fast-intermediate system. These fast-intermediate orbits are what is known as relaxation oscillations: they feature fast excursions to relatively elevated values in v (and the other fast variables, not visible in this projection) alternating with longer epochs where the fast variables are near an attracting branch of fast subsystem equilibrium points, with v near its minimum, and h_{2Na} drifts upward on the intermediate timescale until reaching a saddle-node bifurcation of equilibria of the fast subsystem, where the next spike begins. The spike-free periods of intermediate timescale drift, over which h_{2Na} increases, form the inter-spike intervals as seen in Figure 6A, Region I. The decrease in h_{2Na} during the fast excursion compensates for the silent phase increase in h_{2Na} and ensures that the fast dynamics can return to the attracting branch of fast subsystem equilibria after each spike.

To analyze the gradual increase of h_{NaP} from one spike to the next, we determine the average behavior of h_{NaP} along each of these oscillations using the equation

$$h'_{NaP} = \frac{1}{T(h_{NaP})} \int_0^{T(h_{NaP})} \frac{h_{NaP\infty}(v(t, h_{NaP})) - h_{NaP}}{\tau_{h_{NaP}}(v(t, h_{NaP}))} dt \quad (11)$$

$$h'_{2Na} = \frac{1}{T(h_{NaP}, h_{2Na})} \int_0^{T(h_{NaP}, h_{2Na})} \frac{h_{2Na\infty}(v(t; h_{NaP}, h_{2Na})) - h_{2Na}}{\tau_{h_{2Na}}(v(t; h_{NaP}, h_{2Na}))} dt,$$
(12)

where $v(t;h_{NaP},h_{2Na})$ is the v-coordinate along the stable periodic orbit of the fast subsystem for fixed h_{NaP} and h_{2Na} , with period $T(h_{NaP},h_{2Na})$. Meanwhile, as h_{2Na} drifts downward, the fast variables continue to engage in fast periodic cycles and h_{NaP} remains roughly constant. This pattern of fast voltage oscillations with h_{2Na} progressively decreasing and h_{NaP} relatively constant continues over several spikes. Gradually, however, the rate of change of h_{2Na} slows to become more similar to that of h_{NaP} ; indeed, we have checked numerically that the ratio of $|h'_{2Na}|$ to $|h'_{NaP}|$ drops from $\mathcal{O}(100)$ to $\mathcal{O}(10)$. When they are sufficiently close, we can no longer justify treating them as evolving on separate timescales, and we designate that a transition from Region II (pink) to Region III (cyan) has occurred.

Region III: In this region, the average drift of h_{2Na} becomes smaller in magnitude across successive cycles. Indeed, the difference between Region II and Region III is that in Region III, the change in h_{2Na} becomes so slow that is comparable to the timescale of h_{NaP} . Thus, we no longer consider the fast-intermediate system with h_{2Na} as the unique variable evolving on the intermediate timescale, and we instead treat the full set of model equations as a fast-slow system. Here, h_{2Na} and h_{NaP}

where $v(t, h_{NaP})$ is the stable periodic cycle of the fast-intermediate system for fixed h_{NaP} , with period $T(h_{NaP})$. We compute numerically that the right hand side of equation (11) is positive, and hence h_{NaP} increases slowly in this region.

Therefore, in region I, we observe fast-intermediate timescale oscillations, while h_{NaP} has a slow, increasing drift. Eventually, this drift eliminates the fast-intermediate oscillations (i.e., h_{NaP} exceeds the upper end of the outer green curve in Figure 6B) and thus induces a transition to Region II.

Region II: In this region, the fast-intermediate system no longer has stable oscillations; rather, for each fixed h_{NaP} in this region, this subsystem has a stable equilibrium point corresponding to depolarization block (Figure 6B, elevated h_{NaP}). Because h_{2Na} evolves on a slower timescale than the fast variables, however, we take the further step of performing a timescale decomposition on the fast-intermediate system, with h_{NaP} fixed, to obtain a more detailed understanding of the transient dynamics of the fast-intermediate subsystem. That is, we treat h_{2Na} as a bifurcation parameter and consider the bifurcation diagram of the fast subsystem.

Performing this step for the h_{NaP} values in Region II reveals that there are stable oscillations in the fast subsystem (green curve, Figure 6D). Each of these oscillations passes above and below the h_{2Na} nullcline (black dashed). The net change in h_{2Na} on each cycle is a decrease, as can be seen from Figure 6A and the negative value of the right hand side of the averaged equation

are the slow variables, and the relevant averaged equations become system (10). We compute numerically from this system that the change in h_{NaP} on each cycle is negative. Therefore, in this case, h_{NaP} , like h_{2Na} , drifts downward as the fast subsystem oscillations continue.

Now, for the analysis of Region III, we have two slow variables, h_{NaP} and h_{2Na} . If we fix either of these variables, then we can generate a bifurcation diagram of the fast subsystem with respect to the other; however, it is important to note that any such diagram is simply one point on a continuum of diagrams, parameterized by whichever slow variable was held fixed. For consistency with our analysis of Region II, we will continue to visualize fast subsystem bifurcation diagrams with respect to h_{2Na} with h_{NaP} fixed. Although we will project the trajectory onto such diagrams, it is important to keep in mind that, since h_{NaP} changes at a rate comparable to h_{2Na} in this region, the trajectory actually evolves along a continuum of these diagrams.

Eventually, the slow downward drift of h_{NaP} and h_{2Na} induces a pair of homoclinic bifurcations for the fast subsystem, which split the stable family of periodic fast subsystem solutions (Figure 6D) into two separated families (Figure 6E).

This is the author's peer reviewed, accepted manuscript. However, the online version of record will be different from this version once it has been copyedited and typeset

PLEASE CITE THIS ARTICLE AS DOI: 10.1063/5.0201472

The homoclinic bifurcations first appear at the h_{NaP} value indicated by the dotted green line in Figure 6F; for the part of the cyan trajectory segment to the left of this line, the homoclinic points are present in the fast subsystem bifurcation diagram with respect to h_{2Na} , although the trajectory itself lies at h_{2Na} values below the lower homoclinic point. When these bifurcations occur, the trajectory initially still lies in a region of h_{2Na} on which fast subsystem periodic orbits exist, and oscillations continue. Eventually, however, the drift in (h_{NaP}, h_{2Na}) pulls the trajectory across a fast subsystem homoclinic curve, to where the branch of stable fast subsystem periodic orbits is not present. Thus, the ongoing fast oscillations terminate, and the trajectory jumps on the fast timescale down to the lower, stable branch of fast subsystem critical points (Figure 6E, lower orange trajectory segment transitioning to the neighborhood of the lower red curve, where the trajectory is colored purple).30

Region IV: In this region, the trajectory travels along the lower branch of fast subsystem critical points on the intermediate timescale, with h_{2Na} increasing and h_{NaP} increasing as well, due to the imperfect separation of timescales, but doing so over a relatively small range (note the small change in h_{NaP} in Figure 6A, Region IV, relative to the change in h_{2Na}). This excursion lasts until the trajectory returns to the fast subsystem saddle-node bifurcation. We have indicated where the SN point lies in Figure 6E for $h_{NaP} = 0.215$, using an asterisk and SN label at v below -50 mV and h_{2Na} just above 0.8. Due to the small drift in h_{NaP} in Region IV, the actual jump-up occurs with $h_{NaP} = 0.23$, at the corresponding SN point; this is the point on the SN curve in Figure 6F where the trajectory switches from purple to grey. Once an SN point is reached, the trajectory jumps up to start another phase of spiking oscillations in Region I for the next burst cycle.

We have now analyzed a full ramping burst cycle. The variables h_{2Na} and h_{NaP} are slower than the other variables (fast variables) in the system. Therefore, we can also plot the twoparameter bifurcation diagram of the fast subsystem with respect to h_{2Na} and h_{NaP} (Figure 6F) to gain another viewpoint on the overall burst dynamics. Since h_{2Na} has an intermediate timescale between that of the slow variable h_{NaP} and the other, faster variables in the model, we calculated the averaged nullcline for h_{2Na} (using equation (12)) with h_{NaP} fixed at different values that it takes over the course of the burst cycle. This curve is shown in black in Figure 6F. We also plot the h_{NaP} -nullcline (based on equation (11)) specifically for region I, where there are stable oscillations in the fast-intermediate subsystem, as a dashed black line. Furthermore, the burst trajectory is shown with the same region-by-region color coding used in the other figure panels.

Proceeding region by region, we see that in Region I (grey), h_{2Na} oscillates on each spike but shows little net drift, while h_{NaP} increases across cycles and approaches its nullcline, consistent with Figures 6A-C. The drift in h_{NaP} pulls the trajectory away from the h_{2Na} nullcline, such that h_{2Na} transitions to an epoch of more pronounced downward drift (Region II, pink). There cannot be fast-intermediate periodic solutions when h_{2Na} is behaving in this non-periodic way, matching what we observed in Region II in Figure 6D, and the spikes

here represent fast subsystem oscillations. Since the dynamics in Region II is taking place on the fast and intermediate timescales and does not converge to an attractor of the fast-intermediate system, little change in h_{NaP} can occur in this region.

Due to the shape of the h_{2Na} nullcline (black), the trajectory gradually comes closer to this nullcline and the downward drift of h_{2Na} slows. This effect means that in Region III (cyan), h_{NaP} changes to a similar extent as h_{2Na} across successive fast subsystem oscillations. We checked numerically that the slow averaged drift in h_{NaP} is negative here; the h_{NaP} nullcline from system (10) lies very close to the homoclinic curve, so we do not include it in Figure 6F. This drift in h_{NaP} in turn pulls the trajectory still closer to the h_{2Na} nullcline and slows the drift of h_{2Na} more. As these effects continue, the trajectory (orange segment) reaches and crosses the fast subsystem homoclinic curve (green curve, but overlapped by the black h_{2Na} -nullcline near where the transition occurs), which terminates the fast oscillations and produces the transition to the silent phase (purple). Once this happens, the averaged h_{2Na} nullcline is no longer relevant since there are no fast subsystem oscillations to average around, and the original h_{2Na} equation gives an increase in h_{2Na} , along with a weaker increase in the slower variable h_{NaP} , until the fast subsystem SN curve (magenta) is reached and the next cycle of ramping oscillations begins.

Note that for $g_L=3.54$, the AM spiking solution corresponds to a small amplitude periodic cycle in the (h_{NaP},h_{2Na}) -space that does not intersect the homoclinic curve (Figure 5C). In case of ramping bursting with $g_L=4$, the amplitude of the oscillation in the (h_{NaP},h_{2Na}) -space (intermediate-slow subsystem) has grown large enough that the orbit projection intersects the fast subsystem homoclinic curve (Figure 6F). This corresponds to the termination of the fast subsystem oscillations and a fast transition to a branch of fast subsystem critical points during each burst cycle. Thus, an increase in g_L causes the (h_{NaP},h_{2Na}) oscillation to grow in a way that induces a transition in the model activity pattern from spiking to bursting

G. Fast subsystem oscillations yield a return to tonic spiking in the DSPK model with $g_L=4.6\,$

For $g_L=4.6$, the model exhibits the spiking pattern shown in Figure 7A. These spikes are larger and slower than those arising for $g_L=3.5$. Non-dimensionalization (see subsection II B and supplementary material Figure S2) shows that for $g_L=4.6$, the timescale constant of h_{2Na} is comparable to the timescale of the fast variables in the model, particularly for high ν values that occur near spike peaks. In this case, we analyze the model as having 6 fast variables, including h_{2Na} , and 1 slow variable, h_{NaP} .

Figure 7B shows the bifurcation diagram of the fast subsystem (all variables except h_{NaP}) with respect to h_{NaP} . Notice that the spiking trajectory corresponds to a stable periodic orbit in the fast subsystem for $h_{NaP} \approx 0.33$ (Figure 7C); based on the position of the h_{NaP} nullcline and the evaluation of the

PLEASE CITE THIS ARTICLE AS DOI: 10.1063/5.0201472

right hand side of equation (11), the slow drift in h_{NaP} averages out to 0 on each oscillation cycle.

H. Ramping bursts are robust but pattern details change as g_{Na}, g_{NaP}, g_{syn} vary

In this section, we analyze the robustness of the ramping bursting pattern exhibited by the DSPK model (1), (2) with respect to parameters g_{Na} , g_{NaP} , and g_{syn} . We chose these parameters because g_{Na} and g_{NaP} levels may change over the course of development^{31–34}, while g_{syn} provides a simple representation of the strength of outside inputs including feedback control signals to the neuron, and functional rhythms should be robust to changes in the levels of such inputs.

Figure 8A shows the activity patterns exhibited by the model for various g_{Na} and g_{NaP} values. The default values that we chose for g_{Na} and g_{NaP} are marked with a black dot in Figure 8A. The ramping burst region is shown in red, while the non-ramping bursting (either bursts with fewer than three spikes or depolarization block bursts³⁵ where the active phase of the burst has decaying oscillations and the voltage eventually stabilizes at a sustained, depolarized level) and spiking regions are shown in blue and black, respectively. Interestingly, we see a weak trend in which larger g_{NaP} values are needed to maintain ramping bursts as g_{Na} increases. Thus, I_{Na} and I_{NaP} , although both inward sodium currents, are not compensating for each other, presumably due to the differences in the timescales on which they operate and their correspondingly distinct effects on spike height and frequency. As with Figure 3A, we have used two-parameter continuation of bifurcation curves to generate the boundaries between activity patterns in panel Figure 8A.

The maximum inter-spike intervals within the active phases of the ramping burst patterns are color-coded over the parameter region supporting ramping bursts in Figure 8B. Since spiking frequency usually increases as the ramping burst progresses, the maximum inter-spike interval in the burst is generally the time from the first spike within the burst to the second. The bursting patterns exhibited by the model at g_{Na} and g_{NaP} values sampled along a line through the ramping region are shown as insets in Figure 8B. The maximum inter-spike interval decreases when going from inset Figures (a) to (c), consistent with the color-coding in Figure 8B. Also, notice in the inset figures in Figure 8B that the minimal voltage values change more as each burst progresses in (b) and (c) compared to (a). This property is illustrated in Figure 8C, where the color-code indicates the magnitude of the ramping of the plateau potential, defined by the change, over the duration of the burst, in the minimum voltage attained between spikes.

We also explored the different bursting patterns exhibited by the DSPK model (1), (2) over varying values of g_{syn} (Figure 9). The period of the burst cycle (i.e., active phase plus silent phase) with respect to g_{syn} with (g_{Na}, g_{NaP}) at their default values is plotted in Figure 9A. The inset shows the bursting patterns exhibited by the model for $g_{syn} = 0.3$, 0.33, 0.36, and 0.39. For $g_{syn} = 0.3$, notice that the burst does not ramp but rather features a period of depolarization block, where the

voltage is elevated but no new spikes are generated (as seen in some recordings, cf. 7,36 , and in a previous model 35). As g_{syn} increases from 0.3, the model starts to exhibit ramping bursts. The maximum inter-spike interval and the strength of the ramp (difference in minimal voltages across spikes) in the burst are shown in Figure 9B, C, respectively, for g_{syn} values that give ramping bursts. The burst period, the maximum inter-spike interval, and the the magnitude of ramping all decrease as g_{syn} increases, yielding more gradual, less extreme ramps for larger g_{syn} .

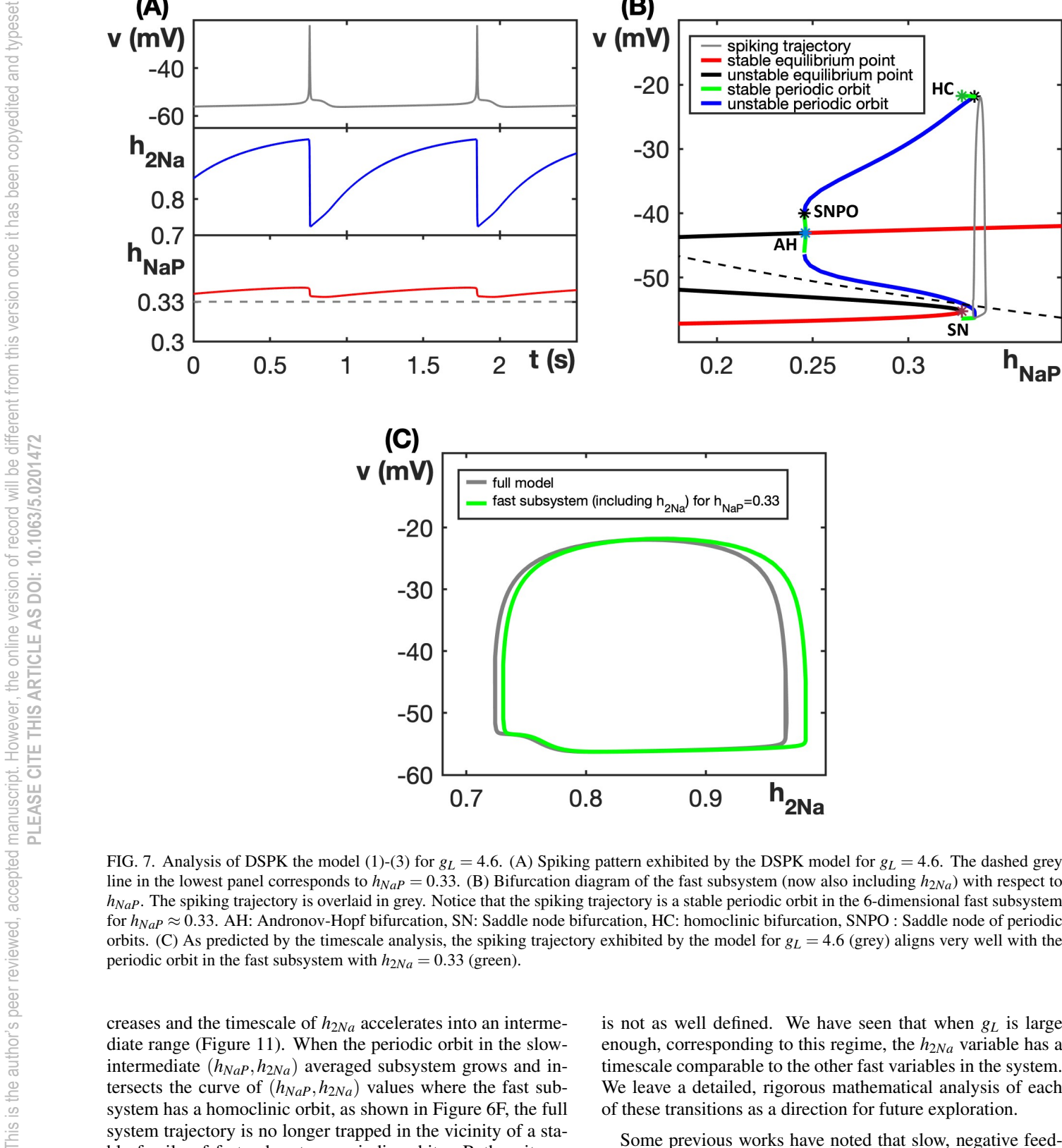
We put these results together, and summarize the activity patterns exhibited by the DSPK model for different g_{Na} , g_{NaP} and g_{syn} values, in Figure 10. Notice that for lower g_{Na} values, ramping burst patterns can arise at lower g_{NaP} and g_{syn} values. As g_{Na} increases, larger g_{NaP} and g_{syn} values are needed for ramping bursts to arise. These results predict that as g_{Na} and g_{NaP} change during development, the range of external feedback signal strengths may need to change as well to preserve functional respiratory dynamics.

IV. DISCUSSION

In this work, we introduce and analyze what we call the DSPK model¹⁶, a neuronal model that includes a secondary, experimentally supported^{22,23} slow negative feedback to the inward sodium current, which induces gradual changes in spike height and an associated ramping effect. The DSPK model produces a range of activity patterns, and we perform dynamical systems analysis based on timescale decomposition to understand how these arise. To begin this process, we observe that non-dimensionalization classifies the persistent sodium inactivation variable h_{NaP} as a slow variable, as in many other pre-BötC neuron models building from the work of Butera et al.³⁷, while most other gating terms are fast variables, meaning that they evolve on approximately the same timescale as the voltage. The timescale of the second inactivation variable of the sodium current, h_{2Na} , depends on the tuning of other model parameters, however, since the model timescales are measured relative to voltage. While always faster than that of h_{NaP} , the h_{2Na} timescale is comparable to that of h_{NaP} when g_L is relatively low, with other model parameters at their default values. On the other hand, when g_L is increased towards and through the ramping burst regime, the timescale of h_{2Na} becomes significantly faster than that of h_{NaP} , in the ramping regime, and eventually is comparable to the timescale of the other fast variables, in a regime where ramping bursts no longer occur.

We analyzed model dynamics for specific, fixed values of g_L , yet our results also give us insights about how transitions between different forms of model dynamics occur. When g_L increases from 3.5 to 3.54, the critical point of the slow averaged nullclines, which corresponds to a spiking solution, becomes unstable through what appears, numerically, to be a supercritical AH bifurcation. As a result, we obtain stable periodic orbits of the slow averaged dynamics in the (h_{NaP}, h_{2Na}) space. These orbits correspond to amplitude modulated (AM) spiking dynamics at $g_L = 3.54$, and they grow in size as g_L in-

(A)



(B)

FIG. 7. Analysis of DSPK the model (1)-(3) for $g_L = 4.6$. (A) Spiking pattern exhibited by the DSPK model for $g_L = 4.6$. The dashed grey line in the lowest panel corresponds to $h_{NaP} = 0.33$. (B) Bifurcation diagram of the fast subsystem (now also including h_{2Na}) with respect to h_{NaP} . The spiking trajectory is overlaid in grey. Notice that the spiking trajectory is a stable periodic orbit in the 6-dimensional fast subsystem for $h_{NaP} \approx 0.33$. AH: Andronov-Hopf bifurcation, SN: Saddle node bifurcation, HC: homoclinic bifurcation, SNPO: Saddle node of periodic orbits. (C) As predicted by the timescale analysis, the spiking trajectory exhibited by the model for $g_L = 4.6$ (grey) aligns very well with the periodic orbit in the fast subsystem with $h_{2Na} = 0.33$ (green).

creases and the timescale of h_{2Na} accelerates into an intermediate range (Figure 11). When the periodic orbit in the slowintermediate (h_{NaP}, h_{2Na}) averaged subsystem grows and intersects the curve of (h_{NaP}, h_{2Na}) values where the fast subsystem has a homoclinic orbit, as shown in Figure 6F, the full system trajectory is no longer trapped in the vicinity of a stable family of fast subsystem periodic orbits. Rather, it can make transitions to transient excursions along the stable lower branch of fast subsystem equilibria. This switch marks the transition from AM spiking to bursting. The additional transition from bursting to tonic spiking when g_L grows further

is not as well defined. We have seen that when g_L is large enough, corresponding to this regime, the h_{2Na} variable has a timescale comparable to the other fast variables in the system. We leave a detailed, rigorous mathematical analysis of each of these transitions as a direction for future exploration.

Some previous works have noted that slow, negative feedback effects can enhance the robustness of specific burst patterns and provide flexibility in burst patterning^{18,38}, but they did not suggest a mechanism for ramping burst generation. Including slow potassium concentration dynamics in a bursting model can result in a ramping burst pattern¹⁴. Compared

An Interdisciplinary Journal of Nonlinear Science

This is the author's peer reviewed, accepted manuscript. However, the online version of record will be different from this version once it has been copyedited and typeset



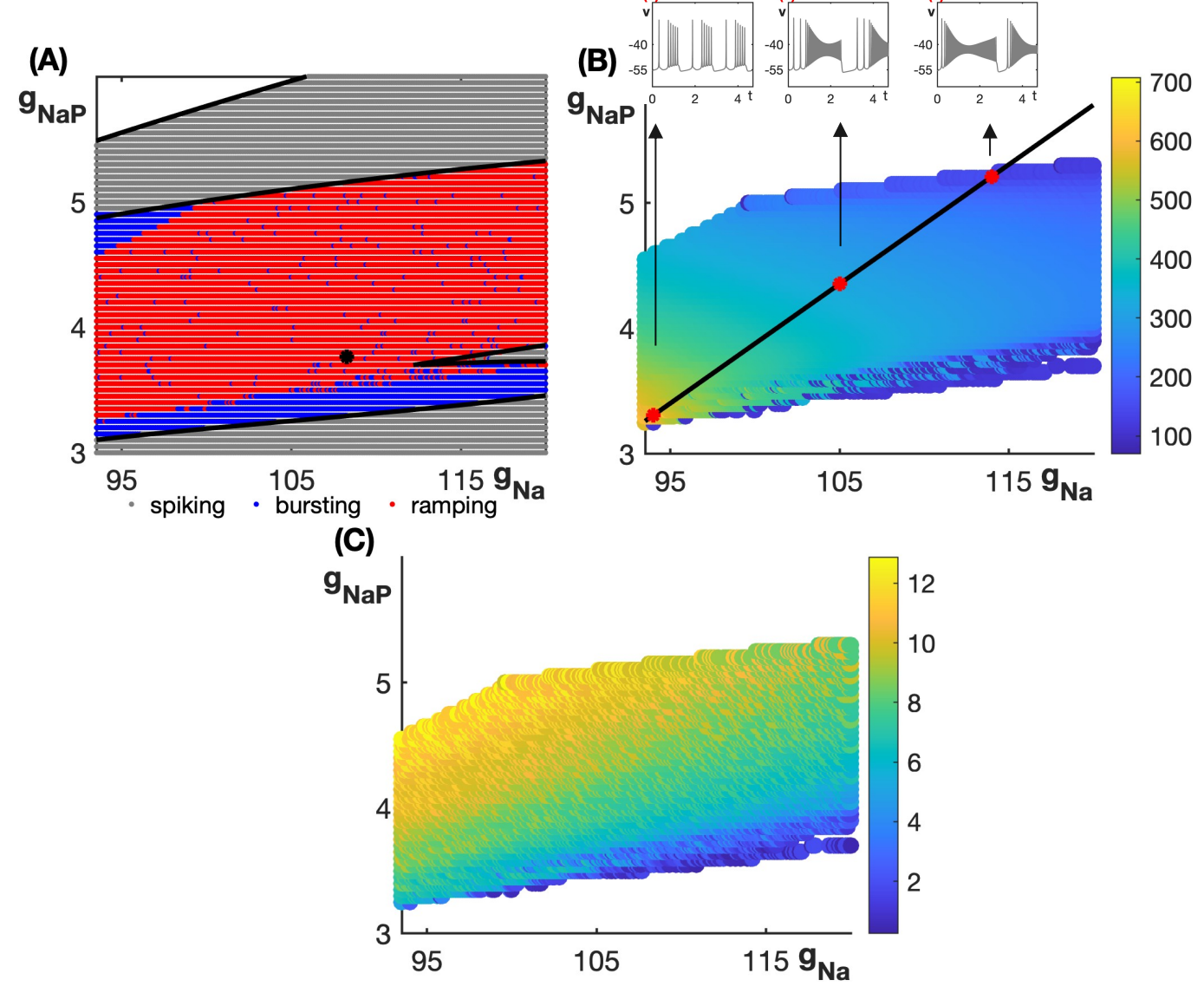


FIG. 8. (A) Bursting patterns exhibited by the DSPK model (1)-(3) over a range of g_{Na} , g_{NaP} values. The black dot marks the default values of g_{Na} and g_{NaP} . The boundaries between the various activity patterns exhibited by the model were determined using two parameter continuation. (B) The maximum inter-spike interval in the ramping burst patterns. (C) The magnitude of the ramp (increase in spike trough voltage level) in the ramping burst patterns.

to that model, the one considered in this work yields ramping bursts with more extreme changes in spike heights across the burst, a feature that has been seen in some experimental recordings⁵, and without the necessity of significant extracellular potassium concentration changes during each burst cycle. These bursts occur over a range of sodium and leak conductances, and one role of feedback input to pre-BötC neurons and of homeostatic adjustments in conductances could be to maintain functionally relevant burst patterning (Fig. 3, Fig. 10). A future direction to explore would be to develop a more detailed model that includes slow sodium inactivation, potassium concentration dynamics, as well as sodium concentration dynamics, to investigate whether the combined presence of these effects further enhances the robustness of ramping

bursts. In another previous paper examining bursting involving recurrent synaptic excitation, calcium dynamics involving I_{CAN} was shown to induce gradual reductions in both the spike height, which led to a decrease in synaptic transmission, and the magnitude of the AHP³⁹, yielding a ramp-like burst pattern with a rather extreme transition from slower tonic spiking to a rapid, decrementing burst of spikes. Including these mechanisms would allow for an even more thorough study of burst patterns. Finally, modeling resurgent Na^+ current is yet another direction to explore in the context of ramping dynamics, since it could enhance inward current flow and lead to faster spiking during each burst⁴⁰; moreover, the possibility has been raised that I_A could contribute to ramping burst patterns⁴¹, which could also be investigated computationally.

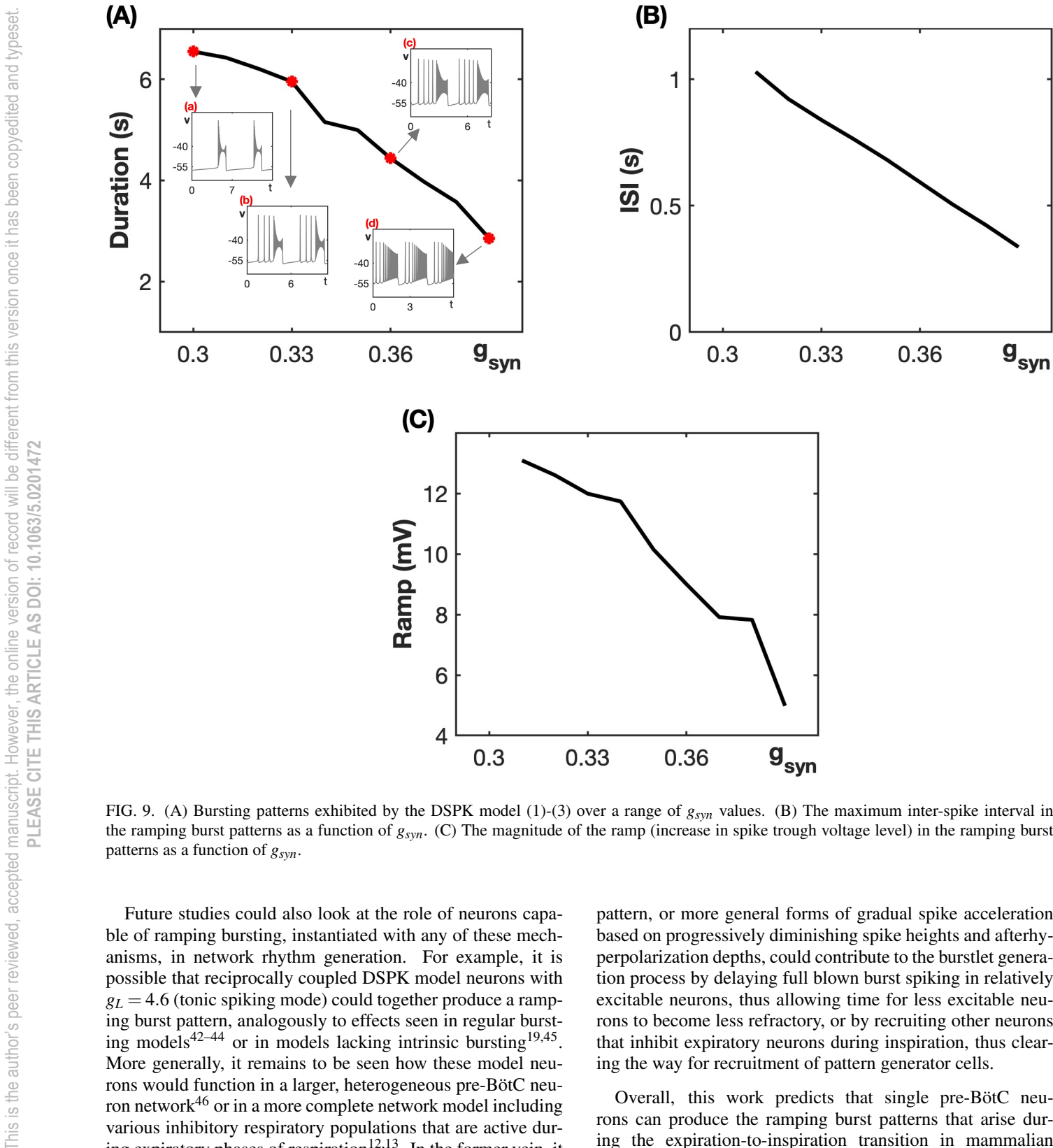


FIG. 9. (A) Bursting patterns exhibited by the DSPK model (1)-(3) over a range of g_{syn} values. (B) The maximum inter-spike interval in the ramping burst patterns as a function of g_{syn} . (C) The magnitude of the ramp (increase in spike trough voltage level) in the ramping burst

Future studies could also look at the role of neurons capable of ramping bursting, instantiated with any of these mechanisms, in network rhythm generation. For example, it is possible that reciprocally coupled DSPK model neurons with $g_L = 4.6$ (tonic spiking mode) could together produce a ramping burst pattern, analogously to effects seen in regular bursting models ^{42–44} or in models lacking intrinsic bursting ^{19,45}. More generally, it remains to be seen how these model neurons would function in a larger, heterogeneous pre-BötC neuron network⁴⁶ or in a more complete network model including various inhibitory respiratory populations that are active during expiratory phases of respiration 12,13. In the former vein, it has been proposed that the respiratory rhythm generator produces relatively small burstlet oscillations, which need to recruit pattern generator neurons in order to transition into a full-blown inspiratory burst⁴⁷. It is possible that the ramping

pattern, or more general forms of gradual spike acceleration based on progressively diminishing spike heights and afterhyperpolarization depths, could contribute to the burstlet generation process by delaying full blown burst spiking in relatively excitable neurons, thus allowing time for less excitable neurons to become less refractory, or by recruiting other neurons that inhibit expiratory neurons during inspiration, thus clearing the way for recruitment of pattern generator cells.

Overall, this work predicts that single pre-BötC neurons can produce the ramping burst patterns that arise during the expiration-to-inspiration transition in mammalian respiration^{7–9,14}. Our work also predicts that, if this activity pattern at the single-neuron level is functionally important, then during development, as sodium channel conductances become stronger, feedback signals to pre-BötC inspiratory neurons should intensify correspondingly. Experiments have the online version of record will be different from this version once it has been copyedited and typeset

PLEASE CITE THIS ARTICLE AS DOI: 10.1063/5.0201472

This is the author's peer reviewed, accepted manuscript. However,

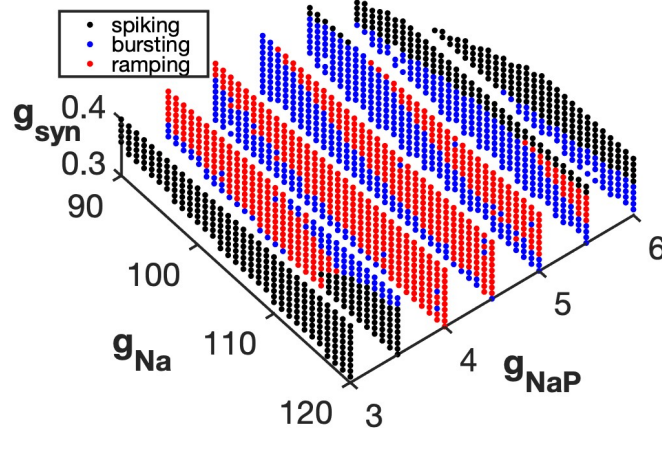


FIG. 10. Classification of activity patterns exhibited by the DSPK model (1)-(3) with variation of g_{Na} , g_{NaP} and g_{syn} values.

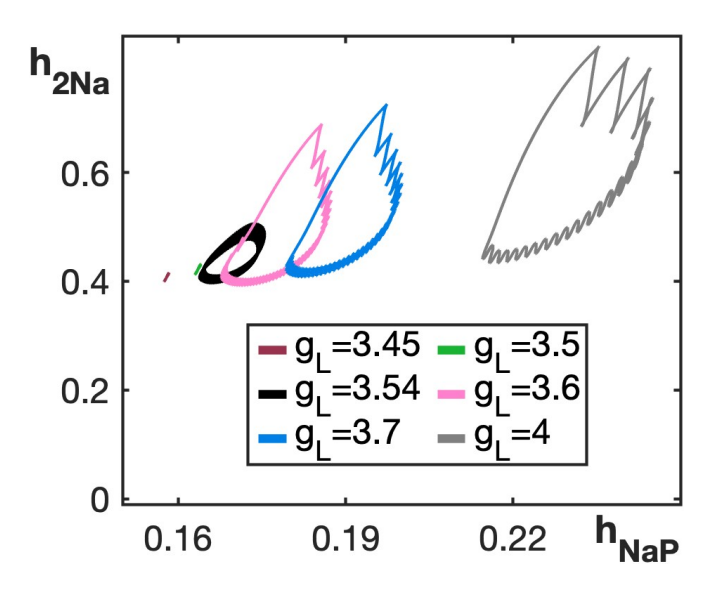


FIG. 11. Projections of the activity patterns of the DSPK model (1)-(3) to $h_{2Na} - h_{NaP}$ space for various values of g_L .

shown that pre-BötC neurons have multiple types of sodium channels, with different kinetics⁴⁸, and the analysis in the paper highlights the potential importance of the timescales of sodium inactivation for shaping neuronal dynamics. Here we find that while the fastest form of sodium inactivation contributes to action potential generation and the slowest form of sodium inactivation, associated with the persistent sodium current, can support bursting, the inclusion of an intermediate inactivation timescale allows for a rich variety of dynamic burst patterns while maintaining robustness of bursting over a range of conductance and input levels, which could allow for flexible modulation of outputs to match functional demands.

SUPPLEMENTARY ONLINE MATERIAL

The supplementary online material comprises two additional figures. One figure shows the ramping burst pattern ob-

tained from rounding the optimal parameter values to the hundreths place. The other shows the magnitudes of the derivatives of several DSPK model variables at various values of g_L .

ACKNOWLEDGMENTS

We thank Victor Matveev of NJIT for assistance with setting up automated parameter optimization for this project. SRJ and JER were partially supported by NSF award DMS1951095. RP was partially supported by NIH award 1K01DA058543-01. SRJ also acknowledges support from the Mathematics Research Center at the University of Pittsburgh. The method and results that we present here are based on an earlier version that appeared in the doctoral thesis of SRJ¹⁶.

AUTHOR DECLARATIONS

Conflict of Interest

The authors have no conflicts to disclose.

Author Contributions

RSP, JER Designed Research; SRJ, JER Performed Research; SRJ, JER Wrote the paper; SRJ, RSP, JER Edited the paper.

Appendix A: Non-dimensionalization

In this appendix, we use non-dimensionalization to determine the timescales of the variables in the DSPK model (equations (1)-(3)). All variables in the model, except for v, are gating variables and hence are dimensionless. To make the voltage variable dimensionless, we set $v = V Q_v$ where Q_v is a constant representing the nominal values of v and $V = v/Q_v$ is dimensionless. The aim is to find constants R_v , $R_{h_{Na}}$, $R_{h_{Na}}$, $R_{h_{Na}}$, $R_{h_{Na}}$, and R_n , such that

$$V' = R_{v} f_{1}(V, h_{Na}, h_{2Na}, m_{Na}, h_{NaP}, m_{NaP}, n)$$

$$h'_{Na} = R_{h_{Na}} f_{2}(V, h_{Na}, h_{2Na}, m_{Na}, h_{NaP}, m_{NaP}, n)$$

$$h'_{2Na} = R_{h_{2Na}} f_{3}(V, h_{Na}, h_{2Na}, m_{Na}, h_{NaP}, m_{NaP}, n)$$

$$m'_{Na} = R_{m_{Na}} f_{4}(V, h_{Na}, h_{2Na}, m_{Na}, h_{NaP}, m_{NaP}, n)$$

$$h'_{NaP} = R_{h_{NaP}} f_{5}(V, h_{Na}, h_{2Na}, m_{Na}, h_{NaP}, m_{NaP}, n)$$

$$m'_{NaP} = R_{m_{NaP}} f_{6}(V, h_{Na}, h_{2Na}, m_{Na}, h_{NaP}, m_{NaP}, n)$$

$$n' = R_{n} f_{6}(V, h_{Na}, h_{2Na}, m_{Na}, h_{NaP}, m_{NaP}, n)$$

PLEASE CITE THIS ARTICLE AS DOI: 10.1063/5.0201472

where the functions f_i are $\mathcal{O}(1)$ for all i, over the relevant ranges of their arguments.

In the main text, we analyze how the dynamics of this model varies with changes in g_L . Thus, we perform non-dimensionalization for the various values of g_L that we use in our analysis, along with the default values of the other parameters given in Table I and $Q_v = 100$, and we obtain the following results.

First, when $g_L = 3.5$, the timescale constants are:

$$R_{v} = \frac{\max(g_{Na}, g_{NaP}, g_{AHP}, g_{K}, g_{L}, g_{syn})}{C_{m}}$$

$$\approx 6.94,$$

$$R_{h_{Na}} = \frac{1}{\tau_{h_{Na}}(V Q_{v})} \in [0.24, 0.744]$$

$$R_{h_{2Na}} = \frac{1}{\tau_{h_{2Na}}(V Q_{v})} \in [10^{-4}, 0.011]$$

$$R_{m_{Na}} = \frac{1}{\tau_{m_{Na}}(V Q_{v})} \in [4.0, 4.78]$$

$$R_{h_{NaP}} = \frac{1}{\tau_{h_{NaP}}(V Q_{v})} \in [10^{-4}, 0.002]$$

$$R_{m_{NaP}} = \frac{1}{\tau_{m_{NaP}}(V Q_{v})} \in [1.0, 3.5]$$

$$R_{n} = \frac{1}{\tau_{n}(V Q_{v})} \in [0.13, 0.49]$$

Note that the timescales for all the variables (except ν) include denominator terms that depend on the range of ν . When g_L increases from 3.5 to 4 and then further to 4.6, the activation and inactivation variables take on a higher range of values to compensate for the increased hyperpolarization. This, in turn, changes the range of values that ν takes, which we check numerically. Evaluating the various functions in (A2) over this range gives the range of possible values for the timescale constants.

The timescale constants for $g_L = 3.54$ remain similar to

(A2). Next, when $g_L = 4$, the timescale constants are:

$$R_{V} = \frac{\max(g_{Na}, g_{NaP}, g_{AHP}, g_{K}, g_{L}, g_{syn})}{C_{m}}$$

$$\approx 6.94,$$

$$R_{h_{Na}} = \frac{1}{\tau_{h_{Na}}(VQ_{V})} \in [0.167, 1.7]$$

$$R_{h_{2Na}} = \frac{1}{\tau_{h_{2Na}}(VQ_{V})} \in [10^{-4}, 0.11]$$

$$R_{m_{Na}} = \frac{1}{\tau_{m_{Na}}(VQ_{V})} \in [4.0, 8.45]$$

$$R_{h_{NaP}} = \frac{1}{\tau_{h_{NaP}}(VQ_{V})} \in [10^{-4}, 0.006]$$

$$R_{m_{NaP}} = \frac{1}{\tau_{m_{NaP}}(VQ_{V})} \in [1.0, 19.20]$$

$$R_{n} = \frac{1}{\tau_{n}(VQ_{V})} \in [0.06, 0.7]$$

Finally, when $g_L = 4.6$, the timescale constants are:

$$R_{v} = \frac{\max(g_{Na}, g_{NaP}, g_{AHP}, g_{K}, g_{L}, g_{syn})}{C_{m}}$$

$$\approx 6.94,$$

$$R_{h_{Na}} = \frac{1}{\tau_{h_{Na}}(VQ_{v})} \in [0.166, 2.07]$$

$$R_{h_{2Na}} = \frac{1}{\tau_{h_{2Na}}(VQ_{v})} \in [10^{-4}, 0.2]$$

$$R_{m_{Na}} = \frac{1}{\tau_{m_{Na}}(VQ_{v})} \in [4, 9.94]$$

$$R_{h_{NaP}} = \frac{1}{\tau_{h_{NaP}}(VQ_{v})} \in [10^{-4}, 0.0079]$$

$$R_{m_{NaP}} = \frac{1}{\tau_{m_{NaP}}(VQ_{v})} \in [1.0, 28.84]$$

$$R_{n} = \frac{1}{\tau_{n}(VQ_{v})} \in [0.058, 0.739]$$

- ¹J. C. Smith, A. P. Abdala, A. Borgmann, I. A. Rybak, and J. F. Paton, "Brainstem respiratory networks: building blocks and microcircuits," Trends in Neurosciences **36**, 152–162 (2013).
- ²R. R. Dhingra, T. E. Dick, W. I. Furuya, R. F. Galán, and M. Dutschmann, "Volumetric mapping of the functional neuroanatomy of the respiratory network in the perfused brainstem preparation of rats," The Journal of Physiology **598**, 2061–2079 (2020).
- ³L. A. E. Koolen, "Effects of Serotonin 1A Receptor Transmission on Neural Control of Respiration," (2021).
- ⁴J. C. Rekling and J. L. Feldman, "Prebötzinger complex and pacemaker neurons: hypothesized site and kernel for respiratory rhythm generation," Annual Review of Physiology 60, 385–405 (1998).
- ⁵P. A. Gray, J. C. Rekling, C. M. Bocchiaro, and J. L. Feldman, "Modulation of Respiratory Frequency by Peptidergic Input to Rhythmogenic Neurons in the PreBotzinger Complex," Science **286**, 1566–1568 (1999).
- ⁶J. L. Feldman and K. Kam, "Facing the challenge of mammalian neural microcircuits: taking a few breaths may help." The Journal of Physiology **593**, 3–23 (2015).

the online version of record will be different from this version once it has been copyedited and typeset

PLEASE CITE THIS ARTICLE AS DOI: 10.1063/5.0201472

This is the author's peer reviewed, accepted manuscript. However,

- ⁷M. Thoby-Brisson and J. M. Ramirez, "Identification of Two Types of Inspiratory Pacemaker Neurons in the Isolated Respiratory Neural Network of Mice." Journal of Neurophysiology 86, 104–12 (2001).
- ⁸A. K. Tryba, F. Peña, and J. M. Ramirez, "Stabilization of Bursting in Respiratory Pacemaker Neurons." Journal of Neuroscience **23**, 3538–3546 (2003).
- ⁹F. Peña, M. A. Parkis, A. K. Tryba, and J.-M. Ramirez, "Differential Contribution of Pacemaker Properties to the Generation of Respiratory Rhythms during Normoxia and Hypoxia," Neuron **43**, 105–117 (2004).
- ¹⁰T. Yamanishi, H. Koizumi, M. A. Navarro, L. S. Milescu, and J. C. Smith, "Kinetic properties of persistent Na+ current orchestrate oscillatory bursting in respiratory neurons." Journal of General Physiology 150, 1523–1540 (2018).
- ¹¹B. J. Bacak, J. Segaran, and Y. Molkov, "Modeling the effects of extracellular potassium on bursting properties in pre-Bötzinger complex neurons." Journal of Computational Neuroscience 40, 231–245 (2016).
- ¹²B. G. Lindsey, I. A. Rybak, and J. C. Smith, "Computational Models and Emergent Properties of Respiratory Neural Networks," Comprehensive Physiology 2, 1619 (2012).
- ¹³Y. I. Molkov, J. E. Rubin, I. A. Rybak, and J. C. Smith, "Computational models of the neural control of breathing," Wiley Interdisciplinary Reviews: Systems Biology and Medicine 9, e1371 (2017).
- ¹⁴M. U. Abdulla, R. S. Phillips, and J. E. Rubin, "Dynamics of ramping bursts in a respiratory neuron model," Journal of Computational Neuroscience 50, 161–180 (2022).
- ¹⁵Y. Okada, S. Kuwana, A. Kawai, K. Mückenhoff, and P. Scheid, "Significance of extracellular potassium in central respiratory control studied in the isolated brainstem-spinal cord preparation of the neonatal rat." Respiratory Physiology & Neurobiology 146, 21–32 (2005).
- ¹⁶S. R. John, Dynamical systems analysis of patterning and robustness of bursts in neuronal models., Ph.D. thesis, University of Pittsburgh (2023).
- ¹⁷L. S. Milescu, B. P. Bean, and J. C. Smith, "Isolation of Somatic Na+ Currents by Selective Inactivation of Axonal Channels with a Voltage Prepulse," Journal of Neuroscience 30, 7740–7748 (2010).
- ¹⁸S. R. John, B. Krauskopf, H. M. Osinga, and J. E. Rubin, "Slow negative feedback enhances robustness of square-wave bursting," Journal of Computational Neuroscience, 1–23 (2023).
- ¹⁹R. Phillips and N. A. Baertsch, "Interdependence of cellular and network properties in respiratory rhythmogenesis," bioRxiv , 2023–10 (2023).
- ²⁰R. Bertram and J. E. Rubin, "Multi-timescale systems and fast-slow analysis," Mathematical Biosciences 287, 105–121 (2017).
- ²¹B. Ermentrout and D. H. Terman, *Mathematical Foundations of Neuro-science*, Vol. 35 (Springer, 2010).
- ²²L. S. Milescu, T. Yamanishi, K. Ptak, and J. C. Smith, "Kinetic Properties and Functional Dynamics of Sodium Channels during Repetitive Spiking in a Slow Pacemaker Neuron," Journal of Neuroscience 30, 12113–12127 (2010).
- ²³ J. L. Ransdell, J. D. Moreno, D. Bhagavan, J. R. Silva, and J. M. Nerbonne, "Intrinsic mechanisms in the gating of resurgent Na+ currents," Elife 11, e70173 (2022).
- ²⁴J. Rubin and M. Wechselberger, "Giant squid-hidden canard: the 3D geometry of the Hodgkin–Huxley model," Biological Cybernetics 97, 5–32 (2007).
- ²⁵Y. Wang and J. E. Rubin, "Multiple timescale mixed bursting dynamics in a respiratory neuron model," Journal of Computational Neuroscience 41, 245–268 (2016).
- ²⁶B. Ermentrout, "Simulating, Analyzing, and Animating Dynamical Systems: A Guide to XPPAUT for Researchers and Students," SIAM 14 (2002).
- ²⁷C. A. Del Negro, N. Koshiya, R. J. J. Butera, and J. C. Smith, "Persistent sodium current, membrane properties and bursting behavior of prebötzinger complex inspiratory neurons in vitro," Journal of Neurophysiology 88, 2242–50 (2002).
- ²⁸L. K. Purvis, J. C. Smith, H. Koizumi, and R. J. Butera, "Intrinsic Bursters Increase the Robustness of Rhythm Generation in an Excitatory Network," Journal of Neurophysiology 97, 1515–1526 (2007).

- ²⁹P. E. Jasinski, Y. I. Molkov, N. A. Shevtsova, J. C. Smith, and I. A. Rybak, "Sodium and calcium mechanisms of rhythmic bursting in excitatory neural networks of the pre-b ötzinger complex: a computational modelling study," European Journal of Neuroscience 37, 212–230 (2013).
- ³⁰In fact, there is a subtlety in that the trajectory can escape from the basin of attraction of the periodic orbit family slightly before reaching a homoclinic point, due to the drift of the slow variables, but the details of this process are beyond the scope of this work.
- ³¹J. R. Huguenard, O. P. Hamill, and D. A. Prince, "Developmental changes in Na+ conductances in rat neocortical neurons: appearance of a slowly inactivating component," Journal of Neurophysiology 59, 778–795 (1988).
- ³²B.-X. Gao and L. Ziskind-Conhaim, "Development of Ionic Currents Underlying Changes in Action Potential Waveforms in Rat Spinal Motoneurons," Journal of Neurophysiology 80, 3047–3061 (1998).
- ³³M. Fry, "Developmental expression of Na+ currents in mouse Purkinje neurons," European Journal of Neuroscience 24, 2557–2566 (2006).
- ³⁴F. Valiullina, D. Akhmetshina, A. Nasretdinov, M. Mukhtarov, G. Valeeva, R. Khazipov, and A. Rozov, "Developmental Changes in Electrophysiological Properties and a Transition from Electrical to Chemical Coupling between Excitatory Layer 4 Neurons in the Rat Barrel Cortex," Frontiers in Neural Circuits 10, 1 (2016).
- ³⁵Y. Wang and J. E. Rubin, "Complex bursting dynamics in an embryonic respiratory neuron model," Chaos 30 (2020).
- ³⁶M. Chevalier, N. Toporikova, J. Simmers, and M. Thoby-Brisson, "Development of pacemaker properties and rhythmogenic mechanisms in the mouse embryonic respiratory network," Elife 5, e16125 (2016).
- ³⁷R. J. Butera, J. Rinzel, and J. C. Smith, "Models of Respiratory Rhythm Generation in the Pre-Botzinger Complex. I. Bursting Pacemaker Neurons," Journal of Neurophysiology 82, 382–397 (1999).
- ³⁸A. Franci, G. Drion, and R. Sepulchre, "Robust and tunable bursting requires slow positive feedback," Journal of Neurophysiology 119, 1222–1234 (2018).
- ³⁹J. E. Rubin, J. A. Hayes, J. L. Mendenhall, and C. A. Del Negro, "Calcium-activated nonspecific cation current and synaptic depression promote network-dependent burst oscillations," Proceedings of the National Academy of Sciences 106, 2939–2944 (2009).
- ⁴⁰A. H. Lewis and I. M. Raman, "Resurgent current of voltage-gated Na(+) channels," The Journal of Physiology **592**, 4825–4838 (2014).
- ⁴¹J. A. Hayes, J. L. Mendenhall, B. R. Brush, and C. A. Del Negro, "4-Aminopyridine-sensitive outward currents in preBötzinger complex neurons influence respiratory rhythm generation in neonatal mice," The Journal of Physiology 586, 1921–1936 (2008).
- ⁴²R. J. Butera, J. Rinzel, and J. C. Smith, "Models of Respiratory Rhythm Generation in the Pre-Botzinger Complex. II. Populations of Coupled Pacemaker Neurons," Journal of neurophysiology 82, 398–415 (1999).
- ⁴³J. Best, A. Borisyuk, J. Rubin, D. Terman, and M. Wechselberger, "The Dynamic Range of Bursting in a Model Respiratory Pacemaker Network," SIAM Journal on Applied Dynamical Systems 4, 1107–1139 (2005).
- ⁴⁴K.-L. Roberts, J. E. Rubin, and M. Wechselberger, "Averaging, Folded Singularities, and Torus Canards: Explaining Transitions between Bursting and Spiking in a Coupled Neuron Model," SIAM Journal on Applied Dynamical Systems 14, 1808–1844 (2015).
- ⁴⁵R. S. Phillips and J. E. Rubin, "Effects of persistent sodium current blockade in respiratory circuits depend on the pharmacological mechanism of action and network dynamics," PLoS Computational Biology 15, e1006938 (2019).
- ⁴⁶R. S. Phillips and J. E. Rubin, "Putting the theory into 'burstlet theory' with a biophysical model of burstlets and bursts in the respiratory prebötzinger complex," Elife 11, e75713 (2022).
- ⁴⁷K. Kam, J. W. Worrell, W. A. Janczewski, Y. Cui, and J. L. Feldman, "Distinct Inspiratory Rhythm and Pattern Generating Mechanisms in the PreBötzinger Complex," Journal of Neuroscience 33, 9235–9245 (2013).
- ⁴⁸ K. Ptak, G. G. Zummo, G. F. Alheid, T. Tkatch, D. J. Surmeier, and D. R. McCrimmon, "Sodium Currents in Medullary Neurons Isolated from the Pre-Bötzinger Complex Region," Journal of Neuroscience 25, 5159–5170 (2005).